
Politecnico di Torino

Politecnico di Torino
Master of Science Course

**Materials Engineering for Industry 4.0**

Academic year 2025/2026

# Development of a Thermally Enhanced Photopolymerizable Hybrid Resin for Additive Manufacturing via Inorganic Nanomaterial Reinforcement

Supervisors:
Prof. Massimo Messori
DR. Camilla Noè

Candidate:
Valentina Nican
S320749

# Abstract

Leading attention has been given to additive manufacturing techniques, specifically those based on vat photopolymerization, especially for the manufacturing of high-resolution polymeric components with complex geometries. Nevertheless, it is important to consider that conventional acrylate-based photopolymer resins commonly show limited thermal conductivity and fair mechanical performance. These characteristics place restrictions on their use in applications relating to heat dissipation or thermal management.

This paper is mainly devoted to the development of a thermally enhanced dual-cure photopolymerizable resin strengthened with inorganic nanomaterials for additive fabrication. The design is based an acrylate–epoxy hybrid system composed of tripropylene glycol diacrylate (TPGDA) as the photopolymerizable matrix on an epoxy–amine network formed by allyl glycidyl ether (AGE) and 4,4′-diaminodiphenyl sulfone (BAPS). The dual-curing procedure integrates rapid UV-induced radical polymerization during printing process with a thermally activated epoxy–amine reaction during post-curing to improve crosslink density and overall material performance

Two types of nanofillers were integrated to improve thermal transport within the polymer matrix. These nanofillers were hexagonal boron nitride (h-BN) and multi-walled carbon nanotubes (MWCNTs) also a hybrid combination of both fillers. The formulations were processed using LCD-based vat photopolymerization. The characterization of their rheological behavior, curing kinetics, thermal stability and mechanical performance were developed through rheology, photo-rheology, Jacobs working curve analysis, DSC, FTIR, TGA, DMTA, tensile testing, and qualitative thermographic analysis.

The results showed that nanofillers incorporation influences strongly the curing behavior and mechanical performance of the system. h-BN strengthened formulations provided the best mechanical performance after thermal treatment, it was also important observing that the highest tensile strength and modulus values occurred while the hybrid filler system displayed intermediate behavior. It is also necessary noting that the reduced light penetration depth in the presence of nanofillers occurred due to scattering and absorption effects, requiring

adjustment of printing parameters but maintaining overall printability. The thermal characterization developed indicated the effective activation of the epoxy–amine curing reaction during post-curing, which gave as a result an increased glass transition temperature and enhanced thermomechanical stability.

Lastly, it is necessary to mention that enhanced heat dissipation behavior in filler-containing formulations was indicated through infrared thermography in comparison to the neat resin matrix. In general, the results show that hybrid dual-cure photopolymer systems strengthened with thermally conductive nanomaterials are an encouraging approach for developing functional proper materials for vat photopolymerization processes in applications requiring improved thermal management.

# Acknowledgment

# Table of contents

# Table of figures

# Chapter 1: Introduction

The rapid development of technology in fields such as microelectronics, computing automotive, and aerospace engineering has provided an escalation in the use of power demands, nevertheless the number of individual components development has diminished progressively. It is also undeniable that there is the need for the investigation related to more compact and functionally integrated devices since there is a growing demand for advanced materials capable to combine multiple functionalities withing limited volumes. Specifically, materials used in these devices must provide a balanced combination of thermal, electrical, and mechanical properties to ensure efficient heat dissipation, structural stability, and reliable performance. With this in mind, additive manufacturing technologies have emerged as a promising approach since they facilitate the fabrication of complex and highly customized geometries that are not easy and sometimes difficult to achieve using conventional manufacturing techniques [1],[2].

This thesis aims to investigate and develop a dual-cure photopolymerizable hybrid resin reinforced with inorganic nanomaterials for use in vat photopolymerization additive manufacturing.

This investigation is based on the desire to fulfill the need to overcome the inherent thermal and mechanical limitations of conventional acrylate-based photopolymer resins, mainly in applications in which the dimensional accuracy and thermal stability are required. Some examples of these applications include electronic packaging elements, LED housings, sensor casings, and functional components used in compact devices, where localized heat buildup can affect operational stability. In order to attend to these needs and challenges, a hybrid formulation strategy is adopted. This strategy combines a UV-curable acrylate matrix with a thermally activated epoxy-amine network to enhance crosslinking density and overall material performance.

Moreover, thermally conductive nanofillers, specifically hexagonal boron nitride (h-BN) and multi-walled carbon nanotubes (MWCNTs), are incorporated into the polymer matrix to promote improved thermal transport pathways while maintaining compatibility with Vat

photopolymerization printing requirements. The potential interdependent effects of combining plate-like and fibrous nanofillers are also explored.

The scope of this work includes:

- Formulation and preparation of hybrid dual-cure photopolymer resins.
- Evaluation of rheological behavior and printability through working curve analysis.
- Investigation of curing behavior and network formation via spectroscopic and thermo-analytical techniques.
- Mechanical characterization through tensile, compression, and dynamic mechanical analysis.
- Qualitative assessment of thermal dissipation behavior using infrared thermography.

It is important to note that the thermal performance evaluation in this study focuses on comparative and qualitative analysis rather than on absolute quantitative measurement of thermal conductivity. The objective is to identify trends and assess the feasibility of nanofiller-reinforced hybrid systems for thermally enhanced additive manufacturing applications.

This thesis seeks to establish a materials engineering framework for the design of thermally enhanced dual-cure photopolymer systems that balances printability, mechanical integrity, and thermal response within the constraints of vat photopolymerization processes.

To achieve the goal of this research work, a review of the theoretical and practical contributions from investigations on this topic and those related are presented below

## 1.1. Additive Manufacturing: Technological Overview

Additive Manufacturing (AM) has become a key technology for advanced engineering applications, enabling the fabrication of complex geometries through a layer-by-layer process directly from digital models, in which the system takes a 2D layer of computer data and rebuilds it into a 3D solid object. In contrast to conventional subtractive and formative manufacturing techniques, AM offers design freedom, mass customization, material efficiency, reduced waste, and shorter production lead times [1],[2].

Over the past decade, the industrial relevance of AM has increased substantially, especially in aerospace, biomedical engineering, automotive, and tooling sectors. This evolution from

prototyping to functional manufacturing has redirected research toward developing materials that meet structural, thermal, and mechanical performance requirements, rather than focusing exclusively on shape accuracy [1],[3]

All AM parts must start with a software model that fully describes the geometry of the surface. This involves obtaining a computer-aided design (CAD) file, which produces a 3D.. This file must be converted into a format compatible with the slicer software. The Standard Triangulation Language (STL) file format, is commonly used as input for the slicer. The slicer processor generates G-Code as output, which the machine controller transmits to the selected manufacturing technology [3],[4]. According to the standards established by the International Organization for Standardization (ISO) and the American Society for Testing and Materials (ASTM), AM technologies are classified into seven categories [6],[7].

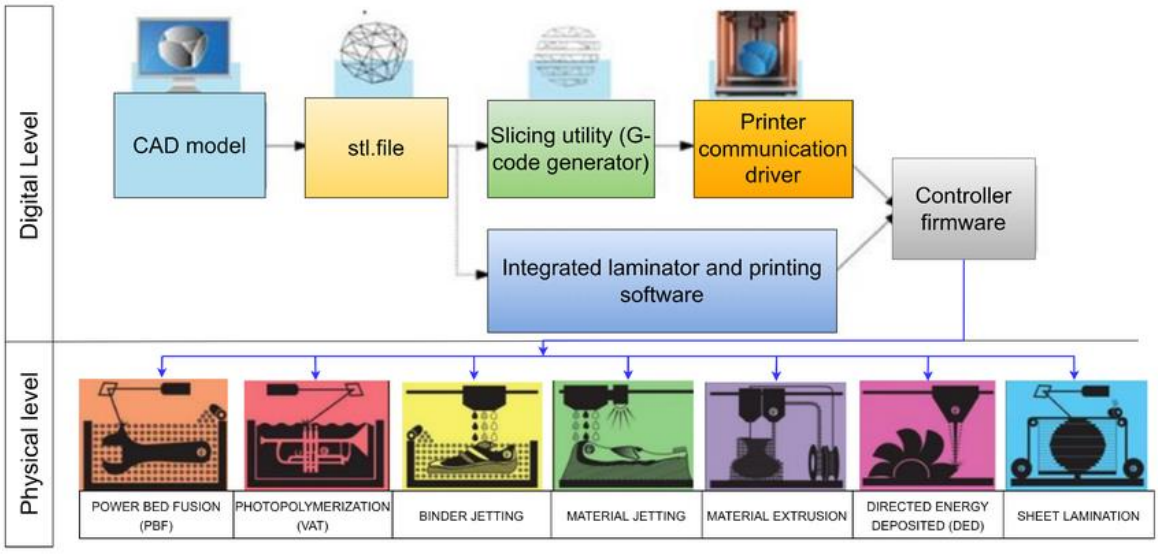


*Figure 1. Additive manufacturing process according to ISO/ASTM 52900 [8].*

Among these technologies, polymer-based additive manufacturing systems are particularly attractive due to their process versatility and relatively low operational costs [3]. Vat photopolymerization (VAT) and fused deposition modeling (FDM) are among the most widely used techniques in both industrial and commercial contexts [9],[10],[12]. While VAT rely on the photopolymerization of liquid resins. For instance, FDM is based on the extrusion of thermoplastic filaments. These technologies differ significantly in terms of achievable resolution, surface finish, and material processing. A comparison of their main characteristics is summarized in *figure 2*.

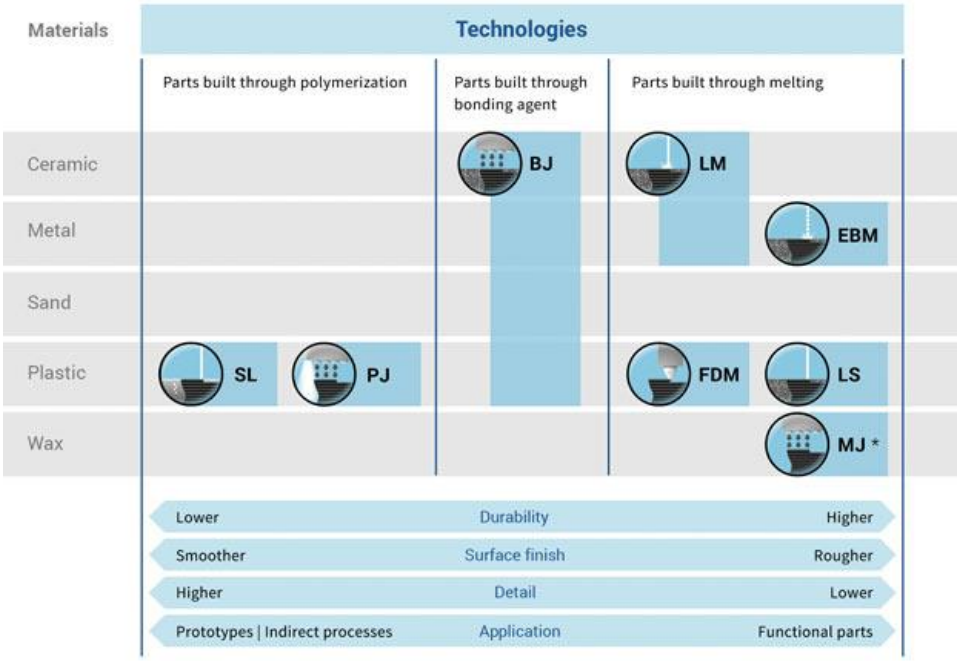


*Figure 2. Overview of 3D printing materials and technologies [9].*

However, the functional performance of polymeric components depends strongly on material formulation and processing parameters. As additive manufacturing advances toward functional and semi-structural applications, the engineering of advanced material systems has turned into a very important research focus.

In this context, vat photopolymerization has attracted significant attention due to its ability to produce parts with high resolution, smooth surface finishes, and excellent dimensional accuracy [3],[9]. The following section focuses on these technologies, with particular emphasis on Liquid Crystal Display (LCD), which constitutes the technological platform investigated in this work.

## 1.2. Vat Photopolymerization Technologies (VAT)

### 1.2.1. Classification and Operating Principles

Vat photopolymerization is one of the most established additive manufacturing technologies for polymer-based materials, characterized by the selective curing of a liquid photopolymer resin through spatially controlled light exposure. In this process, a build platform is progressively raised or lowered within a resin vat while successive layers are polymerized according to the sliced digital model [9],[10][14].

Within VAT, several technologies have been developed, primarily including stereolithography (SLA), Digital Light Processing (DLP), and Liquid Crystal Display (LCD) printing. Although all these techniques rely on photoinitiated polymerization reactions to solidify liquid resins, they differ mainly in the method used to deliver light to the resin and in the way each layer is formed, as illustrated in *Figure 3*.

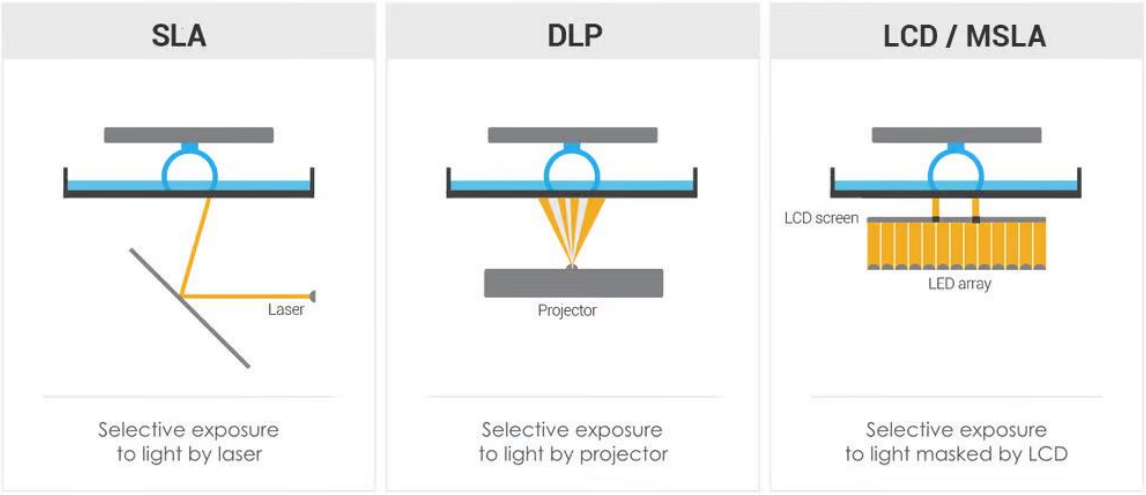


*Figure 3. Different curing methods for vat photopolymerization [11].*

In SLA systems, a focused UV laser scans the resin surface point-by-point to define each layer. This approach offers high precision but may involve longer build times due to the sequential scanning process. In contrast, DLP systems project an entire layer simultaneously using a digital micromirror device (DMD), enabling faster printing speeds while maintaining high resolution [14].

A related and increasingly widespread approach is LCD based vat photopolymerization, which is the technique employed in this work. In this system, a uniform ultraviolet light source is positioned beneath the resin vat, while a liquid crystal display panel functions as a dynamic mask that selectively transmits or blocks light according to the digital pattern of each layer. As a result, an entire layer can be cured simultaneously, similarly to DLP systems; however, instead of micromirrors directing the light, the LCD screen controls exposure at the pixel level by modulating light transmission through individual pixels.[10],[12].

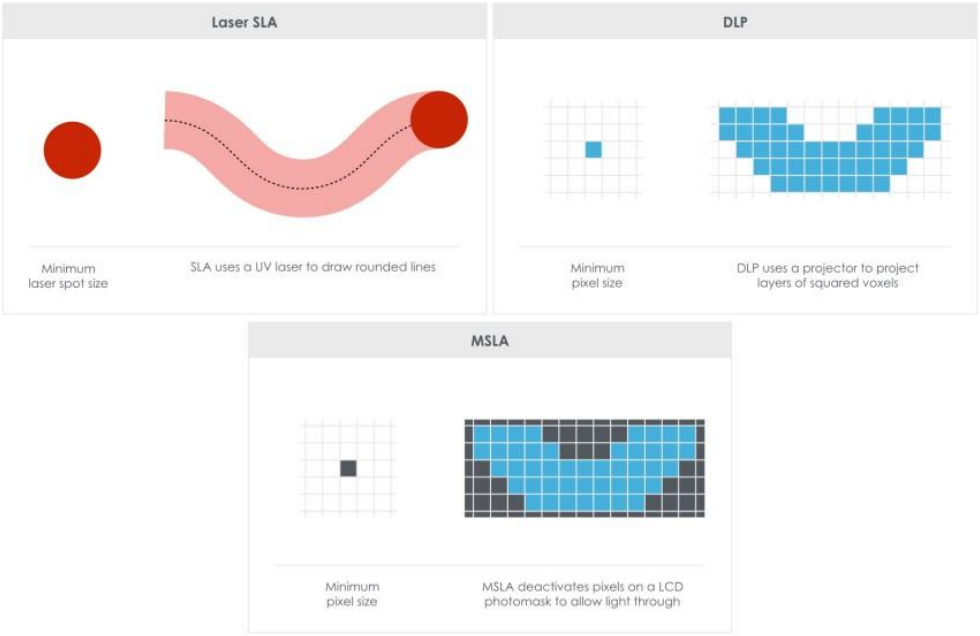


*Figure 4.Accuracy comparison between SLA, DLP and MSLA based on their footprint on building platform, namely, the x-y plane [10].*

Due to this architecture, LCD**,** has become widely adopted in both research and engineering contexts. These systems provide high pixel resolution and allow the fabrication of small, complex geometries with good dimensional accuracy. However, as in other projection-based vat photopolymerization techniques, the printing process is strongly influenced by the optical properties of the resin, including light absorption, scattering, and photoinitiator efficiency, which directly affect curing behavior and dimensional accuracy [10],[14].

Consequently, the formulation of the photopolymer resin plays a critical role in ensuring compatibility between material composition and the processing parameters of LCD additive manufacturing systems.

### 1.2.2. Photo-crosslinking processes

The performance of vat photopolymerization processes is governed by the interaction between incident light and the photoreactive resin. The resin consists of liquid monomers or oligomers that polymerize upon exposure to light of a specific wavelength, forming a crosslinked thermoset network. This process requires a photoinitiator that absorbs the light energy and generates reactive species. This can drive chain growth via radical or cationic

polymerization of epoxides or vinyl ethers, or hybrid reaction mechanisms, which constitute dual curing networks [18].

The polymerization process generally involves three main stages: initiation, propagation, and termination. During the initiation process, the photoinitiator undergoes photolysis upon light absorption, producing free radicals that react with the carbon–carbon double bonds of acrylate monomers. These radicals then propagate through successive addition reactions, forming a crosslinked polymer network until termination occurs by radical recombination or disproportionation [20],[58]. This mechanism enables very short exposure times and high curing rates, which are essential for vat photopolymerization technologies such as Liquid Crystal Display (LCD) printing systems

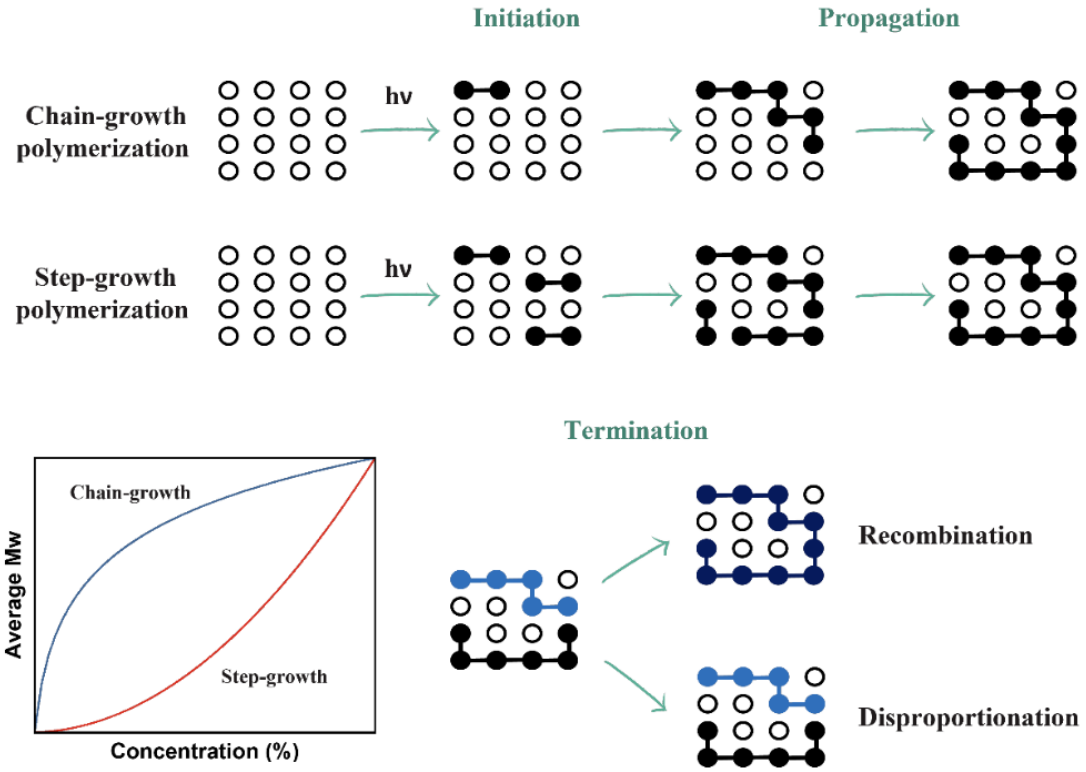


*Figure 5.Polymerization stages involved in the polymer network/chain formation [58].*

Multifunctional acrylates promote the buildup of highly crosslinked three-dimensional networks, providing dimensional stability immediately after curing. This rapid network formation ensures adequate green strength, allowing layer-by-layer fabrication without structural collapse. However, the same high crosslink density often results in brittle

mechanical behavior and limited fracture toughness [18],[20]]. Acrylate systems are susceptible to volumetric shrinkage during polymerization. Radical chain growth reactions proceed rapidly and may generate internal stresses due to non-uniform network formation. These stresses can contribute to warpage, cracking, or reduced dimensional accuracy in printed components [14].

Dual-curing approaches have been increasingly explored to overcome the limitations presented above. It is important to keep in mind that these systems combine two distinct polymerization mechanisms, typically a fast photoinitiated radical reaction followed by a slower thermally activated step-growth reaction, enabling the formation of hybrid or interpenetrating polymer networks [21],[24]. A widely adopted strategy pairs acrylate-based photopolymerization with epoxy–amine thermal curing. Here, the first reaction rapidly fixes the printed geometry, meanwhile the second reaction proceeds during thermal post-curing, increasing crosslink density and improving the mechanical and thermal performance of the material [24],[25],[26].

In the present work, the photopolymerizable matrix is primarily based on tripropylene glycol diacrylate (TPGDA), which undergoes radical photopolymerization initiated by a photoinitiator (TPO-L) under UV exposure during the printing process. In parallel, the formulation incorporates an epoxy component, allyl glycidyl ether (AGE), and an aromatic diamine curing agent (BAPS). During the subsequent thermal treatment, the epoxy groups react with the amine functionalities through a step-growth epoxy–amine curing mechanism, wich form a secondary crosslinked network. This reaction proceeds through the nucleophilic opening of the epoxy ring by the amine groups. Giving way to hydroxyl groups and further crosslinking reactions.

As a result, the system presents two complementary curing processes: a fast radical photopolymerization of acrylate groups during printing, responsible for shape fixation and green strength, and a thermally activated epoxy–amine reaction during post-curing, which enhances network density, mechanical stiffness, and thermal stability. The combination of these mechanisms provides a balanced approach for developing photopolymerizable

thermoset systems suitable for vat photopolymerization while enabling improved final properties in the printed materials.

### 1.2.2. Cure Depth Control

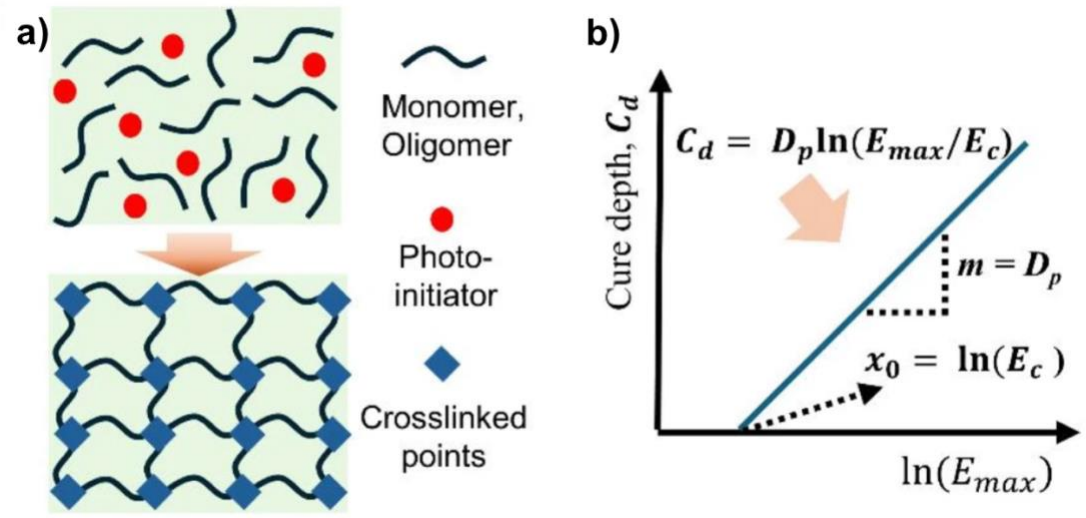


*Figure 6.a) Schematic of the photopolymerization process. (d) Plotting Jacobs working curve and the relationship between the cure depth (Cd), penetration depth (Dp), light energy (Emax), and critical energy (Ec) [18].*

The depth of polymerization depends on several interrelated factors, including light intensity, exposure time, photoinitiator concentration, and the optical absorbance of the resin. As light propagates through the material, its intensity decreases exponentially. According to Beer–Lambert-type attenuation behavior phenomenon directly affects the achievable cure depth and layer thickness [18]. As shown in *Figure 6(b),* the relationship between exposure energy and polymerization depth is commonly described by the working curve model, which defines the critical exposure required to initiate polymerization and the light penetration depth within the resin, can be expressed as Jacobs equation (*Equation 1).* This model is widely used in VAT 3D printing process to calibrate exposure parameters and ensure dimensional accuracy [18],[19].

$$C_d = D_p \ln\left(\frac{E_{max}}{E_c}\right) \qquad \textit{Equation 1}$$

$C_d$: Cure depth.

$E_c$: critical energy; minimum amount of energy needed to start the curing process and reach the gel point.
$E_{max}$: light energy; energy received at the resin surface during the curing.
$D_p$: Light penetration depth in the resin.

Another significant feature of Jacobs' law is that it gives a clue about the inherent parameters of resin, such as critical exposure energy (Ec) and the penetration depth (Dp), which are independent of the specific printer configuration or experimental setup [19]. Nevertheless, it is imperative to regulate the reactivity of the resin so that appropriate optimization of parameters is possible. In the case of nanofillers, the complexity of material-light interaction is further enhanced. Inorganic fillers have a tendency to scatter or absorb light, thus affecting cure depth and adhesion between printed layers. Therefore, there is a need to optimize the content of functional fillers while maintaining transparency.

### 1.3. Inorganic Nanomaterials for Thermal Enhancement

Conventional photopolymer systems exhibit intrinsically low thermal conductivity, typically within the range of 0.1 to 0.3 W/m·K, which is characteristic of amorphous polymeric materials [28],[29]. In such systems, heat transfer is mainly governed by phonon transport; however, the disordered molecular structure and the absence of efficient pathways for thermal energy propagation significantly limit phonon mobility, resulting in poor heat dissipation [31]. This limitation becomes particularly critical in applications involving localized heat generation, thermal gradients, or cyclic thermal loading.

Enhancing the thermal performance of polymeric materials typically involves incorporating thermally conductive fillers that create heat-transfer pathways within the insulating polymer matrix. The introduction of inorganic nanomaterials has merged one of the most extensively investigated strategies to improve thermal dissipation [33].

According to the thermal conduction path and thermal percolation theory, as thermally conductive fillers are incorporated, heat transfer progressively shifts from being dominated by the polymer phase to being influenced by filler–filler interactions. At low concentrations, fillers remain dispersed and isolated, resulting in limited improvement due to interfacial

thermal resistance and phonon scattering. However, as filler content increases, the probability of particle contact rises, enabling the formation of interconnected networks that facilitate more efficient heat propagation across the composite [35].

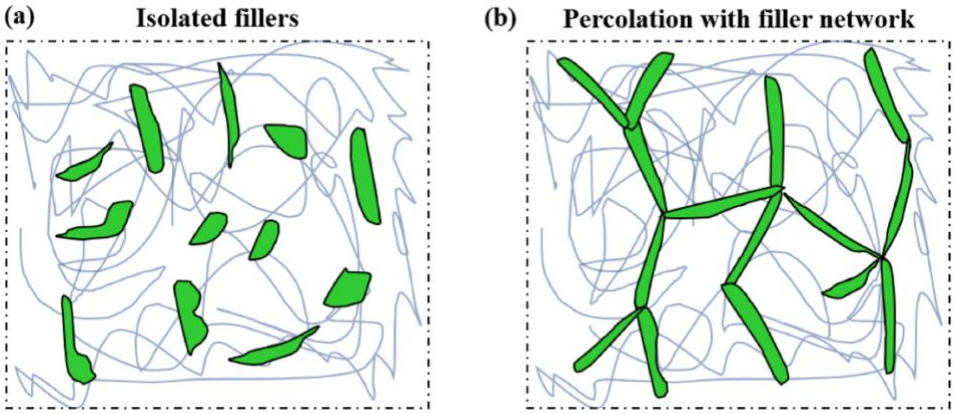


*Figure 7. Nanostructure-embedded polymer host (a) without and (b) with a thermally conductive network formed between nanostructures. The random blue curves in both figures are polymer chains. [27]*

This transition is often described using percolation-based concepts, in which a critical filler concentration leads to the formation of a continuous transport network. While some systems exhibit a distinct threshold behavior, others show gradual improvements depending on filler morphology, orientation, and interfacial compatibility. Therefore, thermal transport in nanofilled polymers is not solely governed by intrinsic filler conductivity but also by microstructural organization and network connectivity within the matrix [34],[35]. High-aspect-ratio fillers are particularly attractive because they can promote the formation of percolated thermal networks at lower volume fractions than spherical particles [36].

The morphology and size of the filler particles play a crucial role in determining the thermal transport behavior of composite materials. The development of two-dimensional or three-dimensional interconnected networks can significantly enhance heat transfer throughout the material. As illustrated in *Figure* 8, fillers with different morphologies can interact within the polymer matrix to form three-dimensional heat-transfer pathways through a so-called “bridging effect.” In comparison with composites containing only a single type of filler, hybrid filler systems facilitate the formation of interconnected thermal networks while requiring lower overall filler content [42].

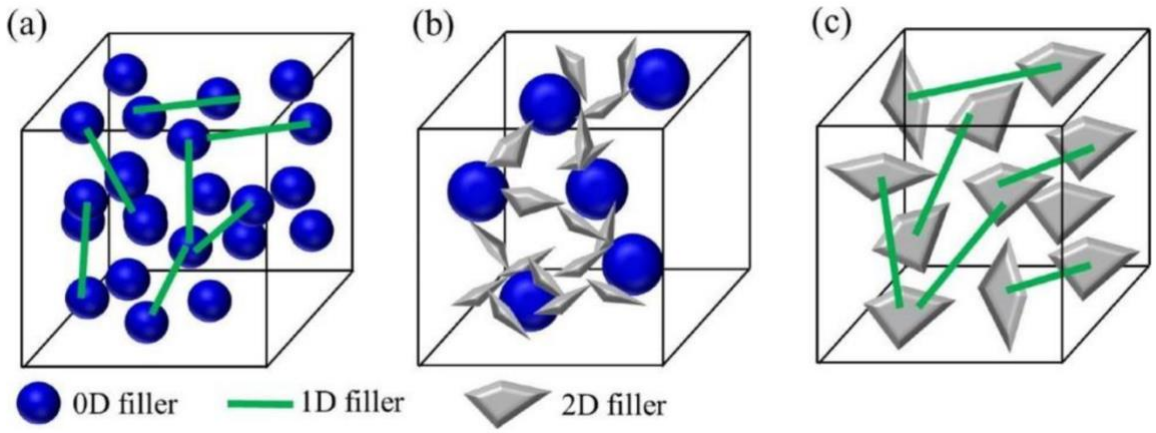


*Figure 8.Schematic diagram of the network formed by the hybrid packings: (a) zero- and one-dimensional fillers, (b) zero- and two-dimensional fillers, (c) one- and two-dimensional fillers [42].*

Among thermally conductive nanomaterials, hexagonal boron nitride (h-BN) and multi-walled carbon nanotubes (MWCNTs) have attracted significant attention for their high intrinsic thermal conductivity and structural anisotropy [33],[34],[35]]. Recent studies suggest that combining fillers with complementary geometries, plate-like h-BN and fibrous MWCNTs may promote the formation of more efficient three-dimensional thermal networks than single-filler systems [33],[34]. In such hybrid systems, MWCNTs can bridge adjacent h-BN platelets, reducing interfacial thermal resistance and facilitating phonon transport across the composite.

Such a synergistic strategy may help in the achievement of improved thermal properties at reduced overall filler loading levels, which is an especially critical challenge for vat photopolymerization systems in which viscosity, light scattering, and cure depth are key parameters. Thus, the use of hybrid nanofillers is an emerging avenue for the development of thermally improved photopolymerizable resins for additive manufacturing technologies.

### 1.3.1. Hexagonal Boron Nitride (h-BN)

Hexagonal boron nitride is a layered ceramic material structurally analogous to graphite, consisting of alternating boron and nitrogen atoms arranged in a hexagonal lattice. It exhibits high in-plane thermal conductivity, making it particularly attractive for applications requiring thermal management. [34],[36].

The platelet morphology of h-BN allows for the formation of two-dimensional heat conduction pathways within polymer matrices *(Figure.*9). These layers are stacked in the through-plane direction, with weak van der Waals forces acting as the binding force. Because of the anisotropic nature of the crystal structure, the thermal conductivity strongly depends on the direction of heat transport. Specifically, the in-plane thermal conductivity (k) is very high, with reported values exceeding 300 $W \cdot m^{-1} \cdot K^{-1}$, whereas the through-plane thermal conductivity is much lower, typically around 3 $W \cdot m^{-1} \cdot K^{-1}$ [37].

However, for effective thermal enhancement, sufficient dispersion and content of the filler must be ensured for effective contact and continuity of phonon transport [36]. On the other hand, excessive content can lead to an increase in viscosity and compromise printability in vat photopolymerization systems.

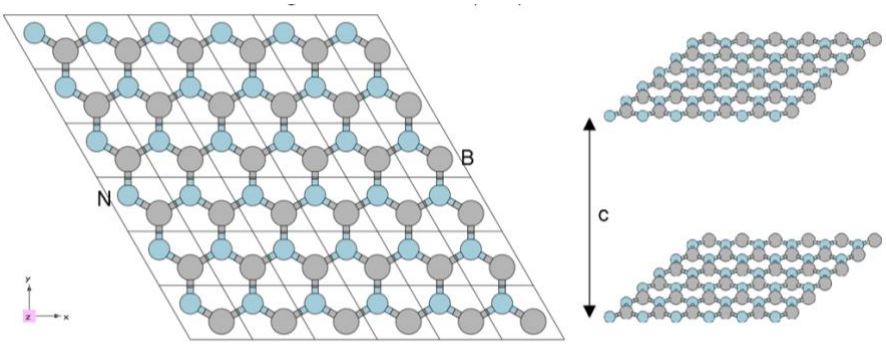


*Figure 9. Hexagonal Boron Nitride (h-BN)-2D sheets.*

### 1.3.2. Multi-Walled Carbon Nanotubes (MWCNTs)

Carbon nanotubes (CNTs) exhibit an outstanding combination of mechanical, electrical, and thermal properties, making them highly attractive as reinforcing fillers in multifunctional polymer nanocomposites [39]. Two primary structural forms of carbon nanotubes can be distinguished: single-walled carbon nanotubes (SWCNTs) and multi-walled carbon nanotubes (MWCNTs). SWCNTs consist of a single graphene sheet rolled seamlessly into a cylindrical structure, whereas MWCNTs are composed of multiple concentric graphene cylinders arranged in a nested configuration, forming a multilayered tubular structure

[40],[41]. A schematic representation illustrating the structural differences between SWCNTs and MWCNTs is presented in Figure 10.

Among these nanostructures, MWCNTs are particularly attractive for polymer composite applications due to their superior structural robustness, easier synthesis, and relatively lower production cost compared to SWCNTs. Furthermore, their high aspect ratio and remarkable intrinsic thermal conductivity along the tube axis, which can reach values of approximately 3000 $W \cdot m^{-1} \cdot K^{-1}$ [42]. Their elongated geometry allows the formation of percolated networks at relatively low filler concentrations, potentially enabling thermal transport improvement with reduced impact on rheological behavior compared to conventional microfillers [36],[40].

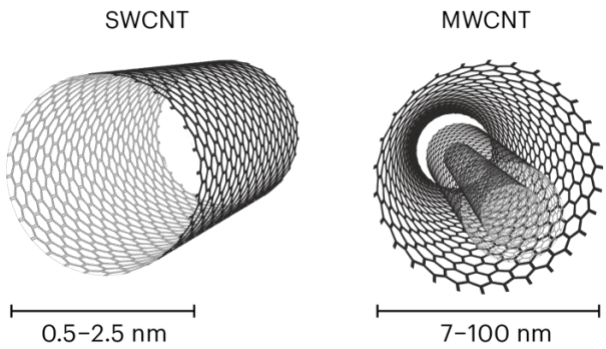


*Figure 10. Schematic representation of a single walled carbon nanotube (SWCNT) and a multi walled carbon nanotube (MWCNT) [41].*

In addition to thermal transport, CNTs can enhance mechanical reinforcement through load-transfer mechanisms between the nanotube surface and polymer chains. However, their dispersion within viscous photopolymer resins remains challenging, and agglomeration may hinder both curing efficiency and final material homogeneity [23].

To place the theoretical framework into practice, chapter 2 deals with the research methodology applied in this investigation.

# Chapter 2: Research methodology

This chapter outlines the methodological approach adopted in the thesis. It describes the materials, formulation strategy, processing parameters, and experimental procedures used to develop and characterize the dual-cure nano-reinforced photopolymer systems investigated in this work.

## 2.1. Materials

The dual-cure photopolymer system developed in this study was formulated using commercially available reagents without further purification. Tripropylene glycol diacrylate (TPGDA) from Sigma-Aldrich was used as the primary UV-curable acrylate monomer; it is a difunctional liquid monomer with a density of approximately 1.03 g/cm³ at 25 °C and was selected to provide rapid radical polymerization and dimensional stability during LCD processing. Allyl glycidyl ether (AGE) was used as the epoxy component; this low-viscosity liquid epoxy monomer has a density of approximately 0.96 g/cm³ at 25 °C and forms a secondary thermally activated network. 4,4′-Diaminodiphenyl sulfone (BAPS) was used as the aromatic amine curing agent for the epoxy phase, contributing to enhancing the thermal stability of the hybrid network. Ethyl (2,4,6-trimethylbenzoyl) phenylphosphinate (TPO-L, IGM Resins) was employed as the photoinitiator due to its strong absorption in the near-UV region (around 385–405 nm), making it suitable for the 405 nm LCD system used in this work. For thermal reinforcement, to enhance the thermal and mechanical properties of the system, nanometric fillers were incorporated, specifically hexagonal boron nitride (h-BN) with an average particle size of 1 μm (Sigma-Aldrich), and multi-walled carbon nanotubes (MWCNT) 50-90 nm diameter, >95% carbon basis (Sigma-Aldrich).

## 2.2. Resin Formulation and Preparation

### 2.2.1. Preparation of epoxy component

The epoxy fraction of the dual-cure resin system was formulated at a stoichiometric ratio of AGE to BAPS. Stoichiometric balance was determined by the equivalence between epoxy groups and active amine hydrogens, as each epoxy group reacts with one active hydrogen

from a primary amine. AGE is a monofunctional epoxide, while BAPS contains two primary amine groups, providing four reactive hydrogens per molecule, as shown in *Figure 11*.

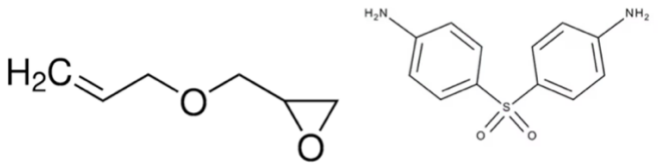


*Figure 11.a) Allyl Glycidil Ether (AGE) , b) 4,4'-Diaminodiphenyl sulfone (BAPS).*

Therefore, the ideal molar ratio is 4:1 (AGE:BAPS). The mixture was stirred magnetically overnight at room temperature to ensure complete homogeneity. The formulation was developed to achieve a thermally stable, mechanically robust material compatible with LCD. For these reasons, AGE was ultimately selected between a range of monomers as the epoxy base, since its lower viscosity and better compatibility with the acrylate phase promoted homogeneous filler dispersion and enhanced printability, enabling easier handling and more reliable layer formation during the LCD printing process [45],[46].

Utilizing a stoichiometric formulation, minimizing unreacted species and promoting the formation of a homogeneous crosslinked network [47]. This method allows for precise control over network architecture and crosslink density, which directly affect the thermal and mechanical properties of the cured system.

### 2.2.2. Preparation of Composite Resins

The formulation of the composite resins was based on previously reported studies that served as a reference for this work [49],[50]. The concentrations of each nanofiller and the ratios of the reactive components were initially set to the optimal values reported in these sources[31],[51].

In the present work, the base formulation consisted of an 80:20 acrylate–epoxy matrix, with 20 wt.% epoxy components relative to the total reactive system. Nanofillers were incorporated according to three configurations: 15 wt% h-BN, 0.1 wt.% MWCNT, and a hybrid formulation containing 15 wt.% h-BN and 0.1 wt.% MWCNT (MIX). The specific compositions of all investigated systems are summarized in *Table 1 and 2*.

*Table 1. Matrix formulation*

| | Wt% | Phr |
|---|---|---|
| **TPGDA** | 80 | |
| **AGE** | 13.5 | |
| **BAPS** | 6.5 | |
| **TPO-L** | | 2 |

*Table 2. content of nano fillers*

| | MWCNTS | h-BN | MIX (MWCNT+h-BN) |
|---|---|---|---|
| **Phr** | 0.1 | 15 | 0.1 + 15 |

To ensure homogeneous dispersion, the nanofillers were gradually added to the liquid resin under continuous magnetic stirring, and the mixture was stirred overnight at room temperature. Following mechanical pre-mixing, four sonication cycles, each lasting 25 minutes. were performed to reduce particle agglomeration. After sonication, the formulations were subjected to an additional 20 minutes of magnetic stirring prior to printing in order to restore flow uniformity and minimize localized concentration gradients.

This combined magnetic stirring and ultrasonic dispersion protocol was selected to improve nanofiller distribution while avoiding excessive thermal buildup or premature reaction.

The 3D printing procedure is described below for a complete exposure about the sequence followed.

### 2.3. 3D Printing Procedure

Specimens were fabricated using a **Phrozen Sonic Mini 8K S** LCD printer operating at a wavelength of 405 nm, with a light intensity of 3.3 mW/cm², according to the producer specifications.

The prepared resin was then poured into the printer vat, and the printing parameters were set according to the selected printing conditions, optimized through preliminary calibration tests of cure depth, analyzed using the working curve approach to determine exposure–penetration relationships for each formulation, as described in section 1.2.2. This evaluation enabled

optimization of exposure parameters to ensure adequate interlayer adhesion and dimensional accuracy. Once the parameters were configured, the printing process was initiated, allowing the samples to be fabricated through the layer-by-layer photopolymerization.


*Figure 12. 3D printer - Phrozen Sonic Mini 8k S, type LC*

## 2.4. Post-Curing Procedure

Post-curing treatment was performed in a Binder convection oven under an air atmosphere. The objective of this treatment was to trigger the epoxy–amine reaction, leading to an enhancement of crosslink density and improving the thermal and mechanical stability of the network.

The temperature ramp was established according to the DSC results, which are discussed in detail in Section 3.5. The complete thermal profile adopted for post-curing is shown in *Figure 13.*

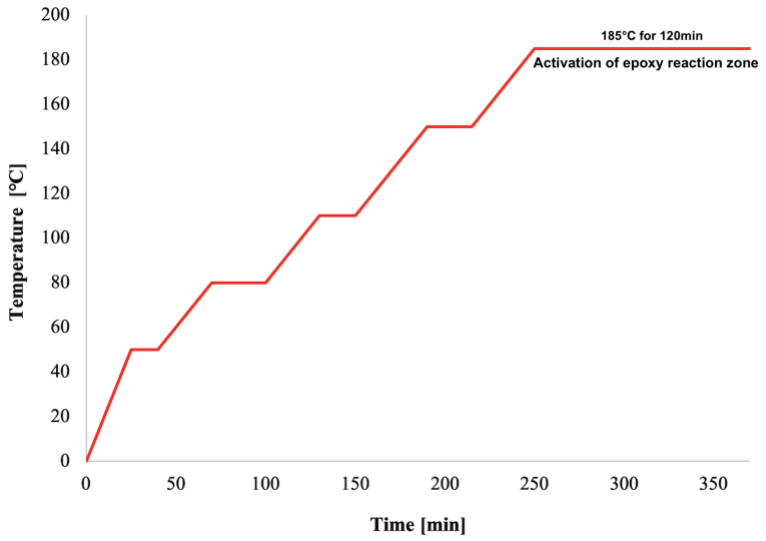


*Figure 13. Heating curve for the thermal treatment of samples.*

## 2.5. Characterization Techniques

The developed formulations were characterized to evaluate their rheological behavior, curing performance, thermal response, and mechanical properties. The selected techniques were chosen to establish correlations between formulation parameters, network formation, and final material performance.

### 2.5.1. Rheological and Photo-Rheological Analysis

Rheological measurements were carried out using the Anton Paar MCR 302(Graz, Austria) rheometer, with a parallel plate geometry to evaluate the viscosity of the prepared formulations and determine their suitability for LCD 3D printing. The dynamic viscosity was measured over a shear rate range from 0.01 to 100 $s^{-1}$. This analysis enabled assessment of flow behavior, filler-induced variations in viscosity, and overall process compatibility.

Photo-rheological experiments were conducted using the same rheometer equipped with a UV light source. The irradiation system operated at a wavelength compatible with the printing setup, delivering an irradiation intensity of 100 $mW/cm^2$ at 100% lamp power. The UV source was activated 30 seconds after the start of each measurement to establish a stable baseline prior to polymerization. The gap between plates was set to 0.3 mm. Measurements were performed at a constant frequency of 1 Hz and at a controlled temperature of 25 °C.

During irradiation, the evolution of storage modulus (G′) and loss modulus (G″) was monitored as a function of time. The storage modulus (G′) represents the elastic component of the material response, while the loss modulus (G″) corresponds to the viscous component.

### 2.5.2. Cure Depth Evaluation (Jacobs Working Curve Method)

The curing behavior of the developed formulations was evaluated using the Jacobs working curve method. During this analysis, the light intensity remained constant at the LCD printer's fixed output (405 nm, 3.3 mW/cm$^2$), while the exposure time was systematically varied.

For each selected exposure time, single-layer samples were fabricated and the resulting cured layers were gently washed with a small amount IPA and left to dry, then the thickness was measured using a digital caliper. The thickness of the cured layer was recorded for each exposure condition to establish the relationship between exposure time and polymerization depth.

The collected data were used to construct the Jacobs working curve by plotting the measured cure depth as a function of the natural logarithm of exposure energy, as explained previously and described in section 1.2.2. Since the light intensity remained constant, variations in exposure energy were controlled by adjusting exposure time. From the linear fit of the experimental data, parameters related to light-penetration depth (Dp) and critical exposure (Ec) were determined, enabling a comparative evaluation of curing behavior among the different formulations.

### 2.5.3. Differential Scanning Calorimetry (DSC)

Differential Scanning Calorimetry (DSC) was employed to investigate the thermal behavior and curing characteristics of the composite resin systems. The analysis was performed on printed specimens. This approach was chosen to evaluate the extent of residual curing reactions remaining after printing and to support the design of an appropriate thermal post-curing protocol.

The DSC measurements were carried out using a DSC 214 Polyma instrument (NETZSCH-Gerätebau GmbH, Germany), with a multi-segment temperature program at a constant heating and cooling rate of 10 $K \cdot min^{-1}$. The samples were initially equilibrated at 25 °C, followed by cooling to −30 °C. Subsequently, a first dynamic heating ramp was performed up to 300 °C in order to evaluate high-temperature thermal events, such as residual curing reactions or the onset of thermal degradation. This heating–cooling sequence was repeated a second time to assess the evolution of thermal behavior and the consumption of residual reactive species during successive thermal scans

### 2.5.4. Fourier Transform Infrared Spectroscopy (FTIR)

Fourier Transform Infrared Spectroscopy (FTIR) analysis was performed using a Nicolet Nexus spectrometer from Thermo Fisher Scientific SL, provided with a Golden Gate ATR sampling accessory. The spectra were recorded in the range of 4000-650 cm−1, performing 16 scans with a resolution of 4 cm−1. The spectra were processed using OMNIC™ Spectra software. This technique was employed to characterize the chemical structure of the formulations and to monitor the conversion of functional groups during polymerization.

For each formulation, the sample was analyzed before polymerization, after 3D printing, and after thermal treatment (TT). In Attenuated Total Reflectance (ATR) configuration, infrared radiation does not pass through the entire sample. Instead, the beam is internally reflected within a crystal in contact with the sample surface, generating an evanescent wave that penetrates only a few micrometers into the material. This allows surface-sensitive analysis without requiring complex sample preparation.

FTIR measurements were conducted to evaluate the degree of polymerization by monitoring the decrease of characteristic absorption peaks associated with reactive groups, particularly the C=C double bonds of acrylate functionalities. The reduction in intensity of these peaks after UV exposure was used as an indicator of conversion and polymerization progress. This approach allowed qualitative assessment of curing efficiency and provided insight into the evolution of network formation following photopolymerization.

The conversion was calculated using the following equation:

$$DC\% = \left[1 - \frac{(A_{c=c}/A_{ref})cured}{(A_{c=c}/A_{ref})uuncured}\right] \times 100\% \qquad \textit{Equation 2}$$

Where $Ac{=}c$ is the peak area of the functional group under investigation during the test and $Aref$ is the peak area used as a reference.

### 2.5.5. Thermogravimetric Analysis (TGA)

Thermogravimetric Analysis (TGA) was performed to evaluate the thermal stability and degradation behavior of the cured formulations. This technique monitors the mass variation of a material as a function of temperature under controlled heating conditions, allowing assessment of decomposition processes.

In this work, TGA analysis was carried out using a Mettler Toledo TGA instrument. Samples weighing approximately 8–10 mg were placed in alumina crucibles and heated from 25 °C to 800 °C at a constant rate of 10 K/min under air atmosphere.

### 2.5.6. Mechanical Testing

The mechanical performance of the printed specimens was evaluated through tensile testing and Dynamic Mechanical Thermal Analysis (DMTA). All measurements were conducted on samples before and after thermal post-curing to assess the influence of the dual-cure treatment on mechanical behavior.

**Dynamic Mechanical Thermal Analysis (DMTA)**

Dynamic Mechanical Thermal Analysis (DMTA) was performed using an Anton Paar MCR 302 rheometer (Graz, Austria) equipped with a three-point bending cantilever configuration.. Evaluating the temperature-dependent viscoelastic behavior of the materials. Rectangular specimens with dimensions of 50 × 120 × 2 mm were analyzed

The temperature sweep was performed from −50 °C to the rubbery plateau region at a controlled heating rate of 5 °C/min. The storage modulus (E′), loss modulus (E″), and damping factor (tan δ) were recorded as a function of temperature. The glass transition temperature (Tg) was determined from the peak of the tan δ curve.

**Tensile Testing**

Uniaxial tensile tests were performed on a Zwick/Roell universal testing machine equipped with a 50 N load cell. The crosshead speed was set to 5 mm/min. Specimens were tested in accordance with ASTM D638, standard tensile testing procedures for polymeric materials (Type I samples). The mechanical response was evaluated by recording stress–strain curves, from which Young's modulus, tensile strength, and elongation at break were determined. For each formulation, at least three specimens were tested to ensure reproducibility, and average values were calculated.

### 2.5.7. Qualitative Thermal Dissipation Analysis

Qualitative thermal dissipation behavior was evaluated using infrared thermography on post-cured specimens. Samples with dimensions (Ø 20× 2 mm) were evaluated.

Each specimen was first placed in a convection oven and heated to 55 °C for 20 minutes to ensure a uniform, stable temperature throughout the sample. Immediately after removal from the oven, the specimen was positioned on a flat, thermally neutral surface, where all samples were placed under identical conditions. The temperature evolution was then monitored using an TR10 MILESEEY infrared thermal imager.

The analysis focused on observing the cooling gradient and temperature decay over time, enabling a comparative assessment of heat dissipation across the different formulations. This approach provides qualitative insight into relative thermal transport performance, rather than absolute thermal conductivity values.

# Chapter 3: Results and Discussion

After the experimentation stages, the results obtained are presented and the discussion on the findings described.

### 3.1. Rheological behavior

The rheological behavior of the developed formulations was evaluated to determine their suitability for DLP processing. *Figure 14* presents the viscosity as a function of shear rate for the neat resin and nanofiller reinforced formulations.

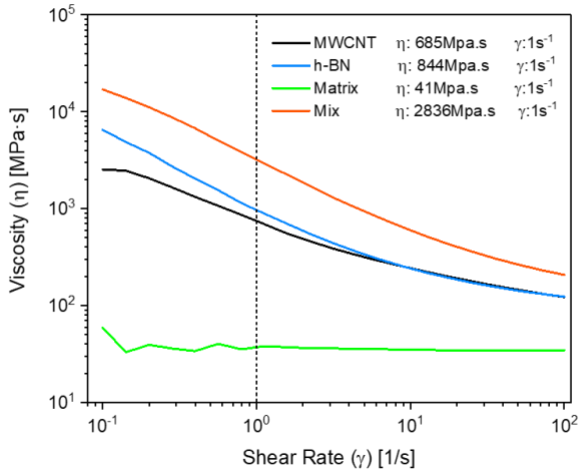


*Figure 14.Effective viscosity vs. shear rate curve for the formulated resins, Average values and related standard deviations for η at γ'=1 s⁻¹ for all formulations prepared.*

The curves demonstrate that matrix formulation shows a Newtonian behavior throughout the tested shear rate range, maintaining a nearly constant viscosity. In contrast, the formulation with content of nano fillers exhibits non-Newtonian behavior, with viscosity decreasing with increasing shear rate, characteristic of shear-thinning (pseudoplastic) behavior, commonly observed in nano-filled polymer suspensions. The interaction between different fillers promotes the formation of a transient, weak particle network within the liquid resin. This network increases resistance to deformation, resulting in higher viscosity at low shear, where van der Waals interactions and physical entanglement among fillers increase resistance to flow.

As can be seen from the reported values, in the *Figure 14*, the addition of ceramic filler increases the viscosity of the resins. The viscosity was measured at a shear rate of 1 $s^{-1}$, arbitrarily selected as the reference value for comparing the effects of the nano fillers on the rheology. MIX shows the highest low-shear viscosity at 2836 mPa.s . followed by the h-BN system, while the MWCNT shows intermediate behavior, and the Matrix resin shows the

lowest viscosity of 41 mPas. This trend is consistent with increasing filler loading and structural complexity within the resin.

In the literature, resins well suited for LCD are typically reported to have viscosities within a broad processing window, often ranging from approximately 0.25 to 10 Pa·s (~250–10 000 mPa·s), with upper limits around 5000 mPa·s commonly cited for filled formulations to maintain adequate flow and recoating without compromising stability or resolution [52],[53]. Viscosity values were found within the range for all formulations, showing suitable processability despite the presence of nanofiller. Interestingly, the shear-thinning response of these filled materials is beneficial for vat photopolymerization, where there is a balance between stability and flowability [53]. At low shear rates, high viscosity reduces filler sedimentation and maintains homogeneous dispersion within the resin. During recoating, however, the applied shear breaks particle networks, reducing viscosity, facilitating rapid resin leveling, and uniform layer formation.

### 3.2. Photo-Rheological analysis

Photorheological characterization was conducted to evaluate the curing kinetics and network formation of the formulated systems under UV irradiation. This analysis provides information regarding the variation of the shear storage modulus (G') as a function of irradiation time (Irradiation was started at 30 seconds) (*Figure 15)*.

Three key parameters can be identified to evaluate the reactivity of the formulation. First, the induction time, which corresponds to the onset of the increase in the storage modulus (G′) curve and indicates the beginning of polymerization. Second, the slope of the rising section of the curve, which directly relates to the crosslinking reaction kinetics and shows how rapidly the network structure develops. Finally, the plateau reached at the upper region of the curve represents the final mechanical properties, providing insight into its stiffness and structural integrity after complete curing. The results are summarized in *Table 4.*

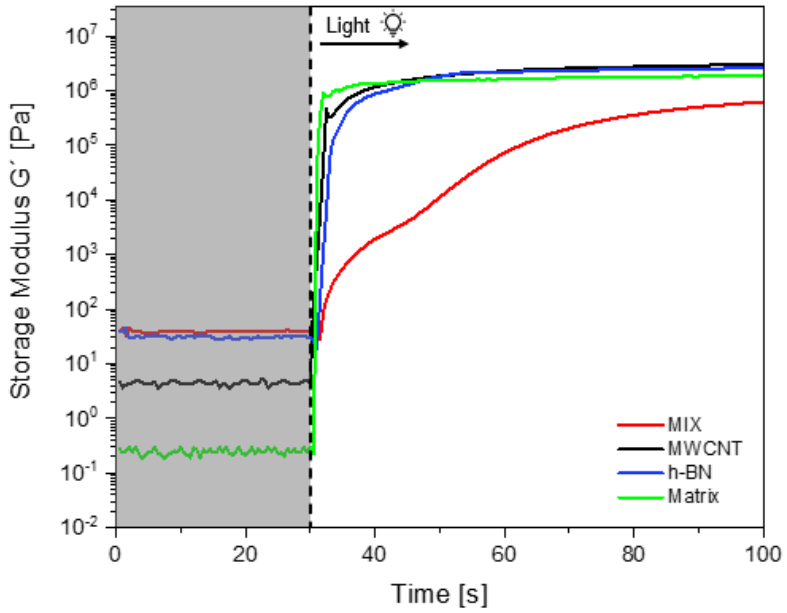


*Figure 15. Photo-rheology curves*

*Table 3.Photo-rheology model parameters*

| | Induction time (s) | Time to plateau (s) | photopolymerization rate (MPa·s⁻¹) | Storage modulus G' (Mpa) |
|---|---|---|---|---|
| **Matrix** | 0 | 40 | 0.88 ± 0.01 | 1.6 ± 0.1 |
| **MWCNT** | 0 | 52 | 0.18 ± 0.09 | 2.2 ± 0.1 |
| **h-BN** | +1 | 57 | 0.16 ± 0.09 | 2.4 ± 0.2 |
| **MIX** | +1 | 90 | 0.02 ± 0.01 | 0.8 ± 0.1 |

As can be seen from the results, *Table 3,* It is possible to observe that immediately upon UV exposure, the matrix and the MWCNT formulation start reacting. This process indicates a rapid radical generation upon light exposure. On the contrary, the minimum delay observed in the h-BN and MIX formulations suggests partial attenuation of UV radiation due to light scattering and/or absorption effects introduced by the inorganic fillers [32].

Likewise, it is possible to notice that when analyzing the time required to reach the plateau and the slope of G', the kinetic differences become more evident, which reflects the rate of crosslinking, following the order: Matrix > MWCNT > h-BN > MIX. This trend is consistent with the progressive reduction in reaction kinetics upon filler addition. It is possible to notice

that the Matrix exhibits the steepest slope, which indicates rapid network formation due to unrestricted radical mobility. The introduction of physical obstacles that limit radical diffusion and chain propagation occur due to the incorporation of fillers. The MIX system, showing the lowest slope of 0.02 MPa.s, suggests additional steric hindrance and possible microstructural heterogeneities that further reduce crosslinking efficiency.

Regarding the storage modulus, the MIX exhibits the lowest final G'. The previous exhibit might indicate that interfacial competition, or incomplete curing resulting from enhanced UV attenuation is the behavior attributed to filler agglomeration. The extended plateau time and reduced slope observed support the hypothesis of a less homogeneous network formation in the hybrid system.

It is possible to state that while individual fillers improve the final elastic modulus, they moderately reduce curing kinetics, after the combined analysis presented. The MIX formulation exhibited the most pronounced kinetic delay and the lowest final modulus. It was possible to provide this anticipated behavior due to the higher filler content and the presence of different types of particles, which can hinder light penetration and reduce curing efficiency under the applied irradiation conditions. Moreover, the dispersion and interaction between fillers influence the rheological behavior of the formulation, wich further affect the photopolymerization kinetics. Taking into consideration LCD processing, it is needed to mention that these findings are particularly relevant since curing rate and network homogeneity directly influence layer adhesion, dimensional accuracy, and printing reliability.

### 3.3. Jacobs Working Curve

This investigation developed additional evaluation on the curing behavior of the developed formulations. This evaluating process took place through the Jacobs working curve method. The relationship between cure depth and the natural logarithm of exposure energy for all systems is presented in *figure 16*. Additionally, the values of penetration depth (Dp) and critical exposure energy (Ec) obtained from the Jacobs working curve analysis are summarized in Table 4.

It is important highlighting the significant differences that can be observed between the Matrix and the formulations containing inorganic fillers since showing that the presence of nanomaterials strongly influences the light propagation and photopolymerization behavior of the system.

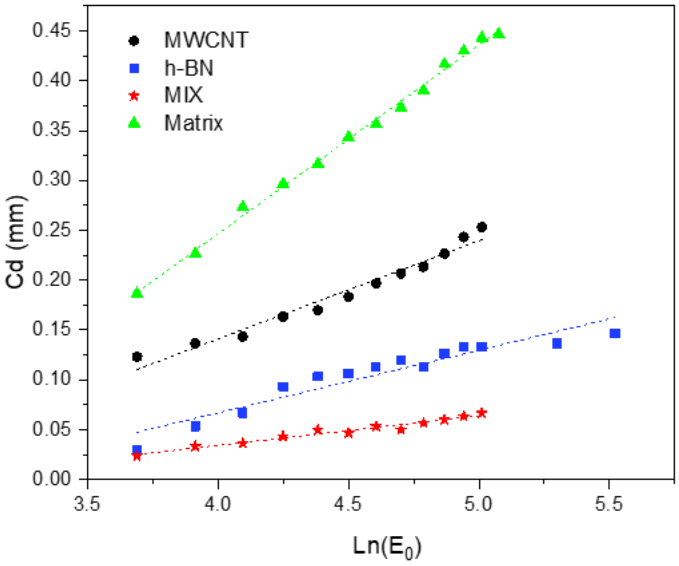


*Figure 16. Jacob's working curve*

*Table 4. Results of curing parameters.*

| | Dp (um) | Ec (mJ/cm2) |
|---|---|---|
| **Matrix** | 190 | 14 |
| **MWCNT** | 98 | 13 |
| **h-BN** | 63 | 19 |
| **MIX** | 30 | 17 |

The highest penetration depth was exhibited by the neat resin matrix, with a Dp value of 189.5 µm, reflecting relatively high transparency and providing efficient light propagation through the material. It is also important mentioning that a marked reduction in Dp was present. This phenomenon is attributed to light absorption and scattering which were caused by the dispersed particles.

It was possible to observe a specifically interesting effect that is typically associated with the refractive index mismatch between the inorganic particles and the polymeric matrix which limits effective light propagation during exposure. This effect is related to the formulation

containing h-BN which showed a substantial decrease in penetration depth to 62.8 μm, suggesting that boron nitride platelets promote light scattering within the resin.

A similar process took place for the formulation containing MWCNT, which showed a Dp value of 98 μm. This occurrence takes into account that carbon nanotubes are known to strongly absorb UV and visible radiation due to their graphitic structure, leading to attenuation of incident light and a reduction in penetration depth compared to the neat matrix.

An outstanding effect was observed in the MIX formulation, in wich the simultaneous presence of h- BN and MWCNT resulted in the lowest penetration depth (30 μm). This behavior suggests a synergistic optical phenomenon where the scattering of h- BN particles and light absorption by carbon nanotubes are limiting the radiation propagation through the resin.

Regarding critical exposure energy, it was observed that the values remained within a narrow range of 13 to 19 mJ/cm $^2$, which indicates that the addition of fillers did not greatly change the minimum energy needed to initiate polymerization. However, a slight increase in Ec was observed for the h- BN and MIX. This is because of the shielding of the photoinitiator molecules by the dispersed particles, which reduced the effective photon flux available for the reaction species.

### 3.4. Selection of printing parameters and validation of printability

Based on the results obtained from the Jacobs working curves, the printing parameters were adjusted to ensure sufficient curing depth and dimensional stability during vat photopolymerization process. The Jacobs analysis provided key information regarding the critical exposure energy (Ec) and the penetration depth (Dp), which were used to estimate appropriate exposure times for each formulation, see *Equation 3*.

$$t_{exp} = \frac{Ec}{I} \times exp\left(\frac{Cd}{Dp}\right) \qquad \textit{Equation 3}$$

Using these parameters as a reference, the final printing conditions were defined to achieve reliable layer-by-layer fabrication. The optimized parameters for printing of each formulation are summarized in *Table 5*.

*Table 5*

| Formulation | Layer Thickness (µm) | Exposure light (mw/cm2) | Bottom Exposure (s) | Normal Exposure (s) |
|---|---|---|---|---|
| **Matrix** | 0.50 | 3.3 | 8 | 6 |
| **MWCNT** | 0.50 | 3.3 | 10 | 7 |
| **h-BN** | 0.35 | 3.3 | 15 | 13 |
| **MIX** | 0.35 | 3.3 | 30 | 28 |

To validate the printability of the developed formulations, test specimens were fabricated under the selected printing conditions. Images of the printed samples are shown in *Figure 17*. The compact specimens, including bars and tensile samples, were successfully printed for all formulations without relevant defects, indicating that the materials exhibited sufficient green strength to maintain their geometry during printing and subsequent handling.

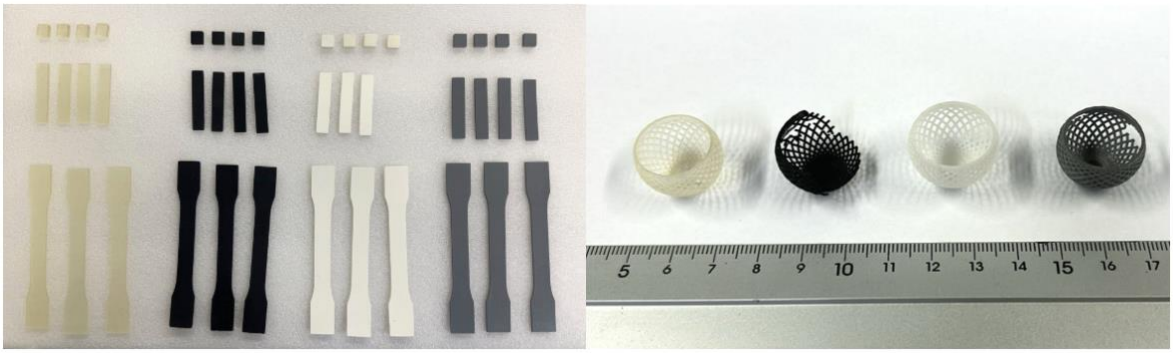


*Figure 16. Printed samples.*

However, when more complex lattice structures were fabricated, differences between formulations became more evident. In particular, the structure printed with the MWCNT formulation showed partial collapse, whereas the h-BN and MIX formulations were able to retain the overall geometry, although some local voids or irregularities were observed. Despite these localized defects, the overall printing quality remained acceptable.

These defects may be related to the long printing times required for complex geometries, during which filler dispersion within the resin may be affected. In particular, sedimentation

or non-uniform distribution of the particles during printing locally influence the curing behavior, leading to incomplete polymerization in certain layers.

### 3.5. DSC

Differential Scanning Calorimetry (DSC) was performed to investigate the thermal curing behavior and network development of the printed formulations. *Figure 18* shows the DSC thermograms obtained for all the formulations during the first and second heating cycles.

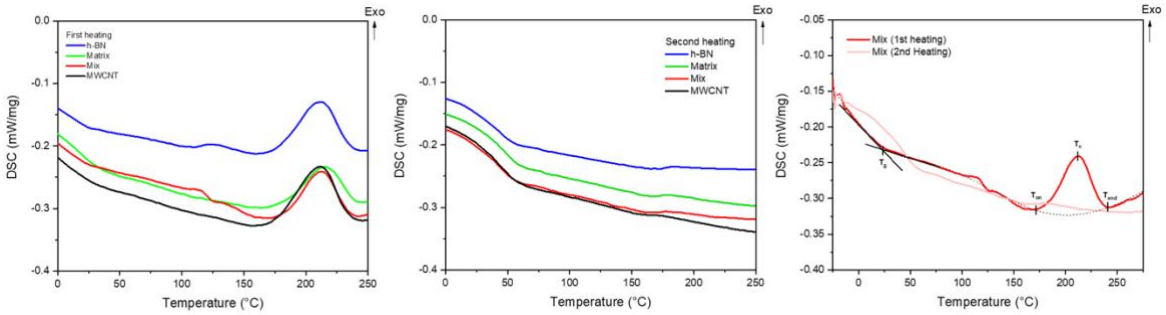


*Figure 17. DSC thermograms of formulations, first and second cycle of heating.*

*Table 6. Characteristic temperatures of the curing behavior.*

| | Tonset [ºC] | Tend [ºC] | Tc [ºC] | Tg [ºC] |
|---|---|---|---|---|
| **Matrix** | 156 | 242 | 211 | 56 |
| **MWCNT** | 162 | 235 | 210 | 53 |
| **h-BN** | 168 | 238 | 212 | 54 |
| **MIX** | 171 | 231 | 213 | 52 |

During the first heating ramp to 300 °C, a pronounced exothermic event was observed in the temperature range between approximately 180 °C and 240 °C, with a peak centered at around 213 °C, The characteristic temperatures of the reaction process are summarized in *Table 6*. This exothermic signal is associated with the thermally activated epoxy–amine reaction occurring in the hybrid dual-cure system.

In the second heating cycle, this exothermic peak disappears, confirming that the curing reaction was completed during the first heating step. This behavior demonstrates that the thermal epoxy-amine reaction was complete.

In addition, the temperature range associated with this exothermic reaction provides a guideline for identifying the temperature window in which the epoxy–amine reaction

becomes active. The DSC results were used to determine the appropriate post-curing thermal treatment applied to the printed specimens.

### 3.6. FTIR

At this stage, Fourier Transform Infrared Spectroscopy (FTIR) helped to investigate chemical changes occurring during the photopolymerization and to test the degree of acrylate conversion after printing (DC-p%) and after thermal post-curing (DC-tt%), The conversion of the acrylic group was also calculated between the UV cured sample and the post thermal treated sample (DC-ep%). *Figure 19* shows the ATR-FTIR spectra that resulted, highlighting the characteristic absorption bands related to the reactive functional groups.

It is worth observing that the uncured formulations show the typical bands of absorption related to the functional groups of the resin. In particular, the stretching vibration of the acrylate double bond (C=C) is found in the region between 1640 and 1618 $cm^{-1}$. In the case of the formulations subjected to the UV radiation during the printing process, a clear reduction in the intensity of this peak is noticed. This aspect demostrates the reaction of the C=C bonds and the formation of the crosslinked polymer network. To quantify the degree of conversion, the variation of the C=C peak intensity is normalized using the C-O stretching band situated between 1850 and 1700 $cm^{-1}$ as an internal reference. This signal remained relatively unchanged during the photopolymerization process for all formulations.

In addition to the acrylate functional groups, the FTIR spectra provide evidence of the epoxy group, determined by a characteristic absorption band located around ~809 $cm^{-1}$**.** The evolution of this band gives important information regarding the epoxy–amine reaction developing while the thermal curing stage. Following the thermal treatment, as shown in *Figure 19, Area (B),* a notable reduction in the 808 $cm-1$ peak was detected, validating the effective opening of the epoxy ring. Concurrently, a new absorption peak appeared at 779 $cm-1$ associated with the bending and stretching vibrations.

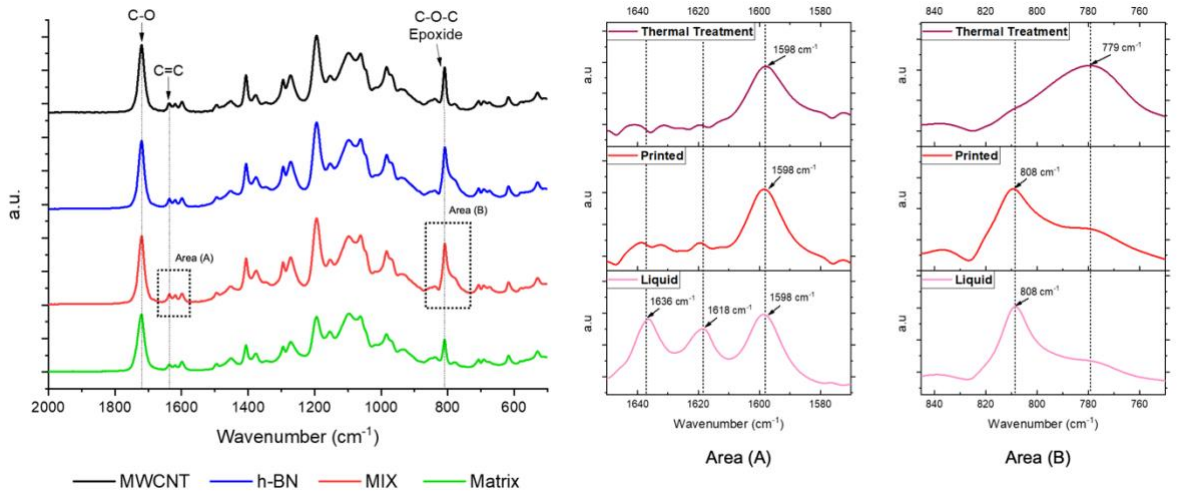


*Figure 18. FTIR spectra before UV curing for each formulation, area (A) shows the peaks of the C=C bonds before UV curing, after, and post TT, area (B) shows the peaks for the epoxy component, before UV curing, after, and post TT.*

*Table 8. Conversion of the acrylate groups, after UV curing (DC-p%), post thermal treatment sample (DC-tt%).*

| | **MWCNT** | **h-BN** | **MIX** | **Matrix** |
|---|---|---|---|---|
| **DC-p%** | 49 ± 15 | 69 ± 2 | 64 ± 3 | 74 ± 19 |
| **DC-tt%** | 88 ± 3 | 94 ± 1 | 70 ± 1 | 81 ± 4 |
| **DC-ep%** | 73 ± 6 | 87 ± 1 | 81 ± 1 | 79 ± 3 |

The calculated values for all formulations are summarized in *Table 6.* The degree of conversion (DC) of the acrylate groups was calculated by comparing the relative intensity of the C=C peak before and after curing, following the *equation 2,* described in the section 2.5.3. The matrix exhibited the highest conversion value after printing 74%, indicating efficient photopolymerization of the acrylate network in the absence of fillers. In contrast, the formulation containing MWCNTs showed the lowest conversion 49%, which is attributed to the strong light absorption properties of carbon nanotubes. Due to their high aspect ratio and optical absorption, MWCNTs can attenuate the incident radiation and reduce the effective photon flux reaching the photoinitiator, leading to slower polymerization kinetics [54]. The formulation containing h-BN showed a relatively high conversion after printing, suggesting that although the platelet morphology of h-BN induces light scattering, its effect on curing efficiency is less pronounced than the light absorption caused by carbon nanotubes [20],[49],[55]. The hybrid formulation containing both fillers presented an intermediate conversion, which can be attributed to the combined effects of light scattering from h-BN and light attenuation from MWCNTs.

After the thermal post-curing, different trends were observed for the formulations. The h-BN system showed the highest acrylate conversion, reaching 94%, which confirms that the photochemical and thermal curing process allows for a more complete development of the polymer network. An increase in conversion was also observed for the hybrid system, suggesting that residual reactions continue during the thermal treatment. Similarly, the MWCNT formulation displayed a moderate increase in conversion, indicating that the post-curing stage partially compensates for the reduced photopolymerization efficiency observed during printing.

As an additional remark, the results of the epoxy conversion revidenced a clear dependence on the type of nanofiller incorporated included into the system. The lowest degree of conversion was observed in the formulation with the following percentages from the lowest to the highest ones, MWCNT (73%), followed by the pure matrix (79%), the hybrid system (81%), and, finally, the sample with h-BN, which exhibited the highest conversion (87%).
The decreased conversion in the presence of MWCNT can be linked to its strong interfacial interactions with the polymer matrix. This fact restricts chain mobility and hinder restricts the diffusion of reactive species during the curing process.
Moreover, the high aspect ratio and tendency to form conductive networks can bring about localized energy absorption and reduced curing performance [61],[62], On the contrary, the incorporation of h-BN fosters a higher degree of conversion. This highly conversion takes place, due to the characteristics of h-BN as having a chemically inert nature and the ability to enhance thermal transport within the system, which permits a more uniform curing process [63]. The hybrid formulation exhibits intermediate behavior, resulting from the \ interaction between the mobility-restricting effect of the MWCNTs and the refinement in thermal conductivity provided by h-BN.

### 3.7. DMTA

Dynamic Mechanical Thermal Analysis was performed to investigate the viscoelastic behavior of the developed formulations and to evaluate the effect of thermal post-curing on the mechanical properties of the materials. The glass transition temperature (Tg) was determined from the peak of the tan δ curve, while the storage modulus (E′) was evaluated

in the rubbery region at 80 °C. The results obtained for the samples after printing and after thermal treatment are summarized in *Table 7*.

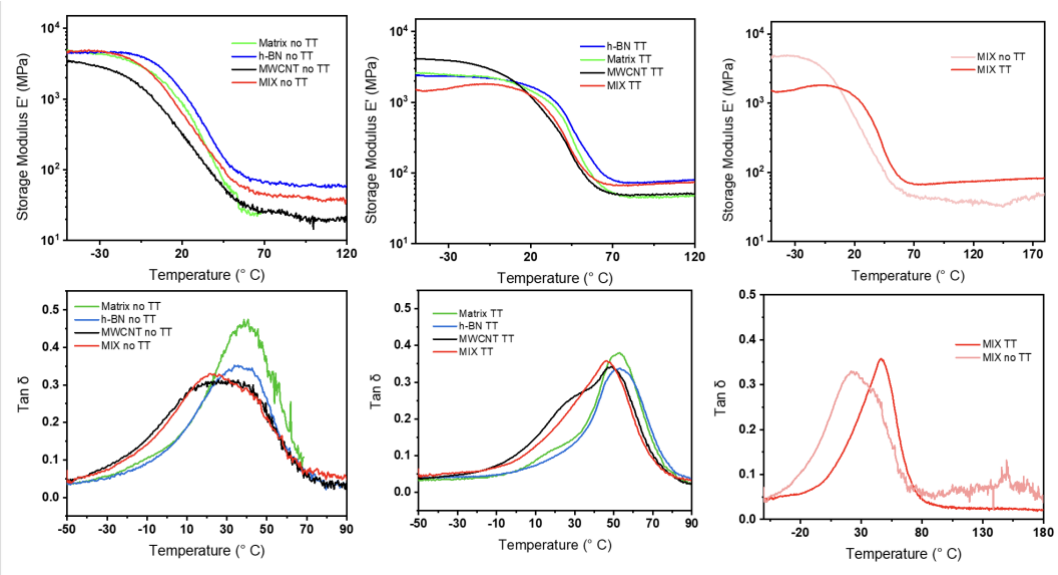


*Figure 19. DMTA thermomechanical response of the printed formulations, showing the storage modulus (E') evolution and the glass transition temperature (Tg) peak for untreated and thermally treated samples.*

*Table 9. Summary of DMTA results: glass transition temperature (Tg) and storage modulus (E') for all formulations before and after thermal treatment.*

| | Tg [ºC] | Tg TT [ºC] | E' [MPa] | E' TT [MPa] |
|---|---|---|---|---|
| **Matrix** | 39 | 52 | - | 45 |
| **h-BN** | 36 | 53 | 65 | 73 |
| **MWCNT** | 27 | 48 | 47 | 24 |
| **Mix** | 23 | 47 | 43 | 67 |

The results show a clear increase in Tg after thermal treatment for all formulations. This increase in glass transition temperature indicates that the thermal treatment promotes additional crosslinking reactions within the polymer network. The results are consistent with the residual curing behavior previously observed in DSC and with the disappearance of the epoxy peak detected by FTIR analysis. These results confirm that the dual-cure system successfully lead to an enhancement of the thermomechanical performances of the 3D printed materials.

The larger Tg increase observed for the MWCNT formulation system suggests that the initial UV curing was less efficient in these systems. This behavior is consistent with the FTIR

results, which showed a lower degree of acrylate conversion after printing in the presence of MWCNTs. Carbon nanotubes are known to absorb UV and visible light, thereby reducing the effective photon flux reaching the photoinitiator and limiting the extent of photopolymerization during the printing process[42],[60]. In addition, weak interfacial interactions between the nanotubes and the polymer matrix introduce interphase regions with increased free volume and enhanced chain mobility, explaining the lower Tg values compared to the other systems.

The storage modulus values measured in the rubbery region at 80 °C, where the viscoelastic response of the materials becomes more stable and the influence of the network structure can be more clearly observed.

Before thermal treatment, the h-BN formulation exhibited the highest storage modulus 65 MPa, indicating the reinforcing effect of the ceramic filler and its contribution to the stability of the polymer network at elevated temperatures. The MWCNT formulation showed a lower modulus 47 MPa, while the MIX system presented a slightly lower value 43 MPa, suggesting that the presence of carbon nanotubes and the hybrid filler system may influence the network formation during photopolymerization.

After thermal treatment, the viscoelastic behavior of the materials changes due to the conversion of the epoxy–amine curing reaction, which leads to an increase in the effective crosslink density of the system. As a result, the storage modulus increases for most formulations, particularly for the h-BN 73 Mpa and MIX 67 MPa systems. This improvement confirms that the post-curing step contributes to further network development and enhances the thermomechanical stability of the materials. In contrast, the MWCNT formulation shows a reduction in modulus after thermal treatment 24 MPa, related to differences in filler dispersion and the influence of nanotubes on the curing process

### 3.8. TGA

Thermogravimetric analysis (TGA) was carried out to evaluate the thermal stability and degradation behavior of the cured formulations. *Figure 21* presents the thermogravimetric curves for the investigated systems, showing the mass loss as a function of temperature. All formulations exhibit a similar degradation profile, characterized by a main weight-loss region associated with the thermal decomposition of the polymeric network.

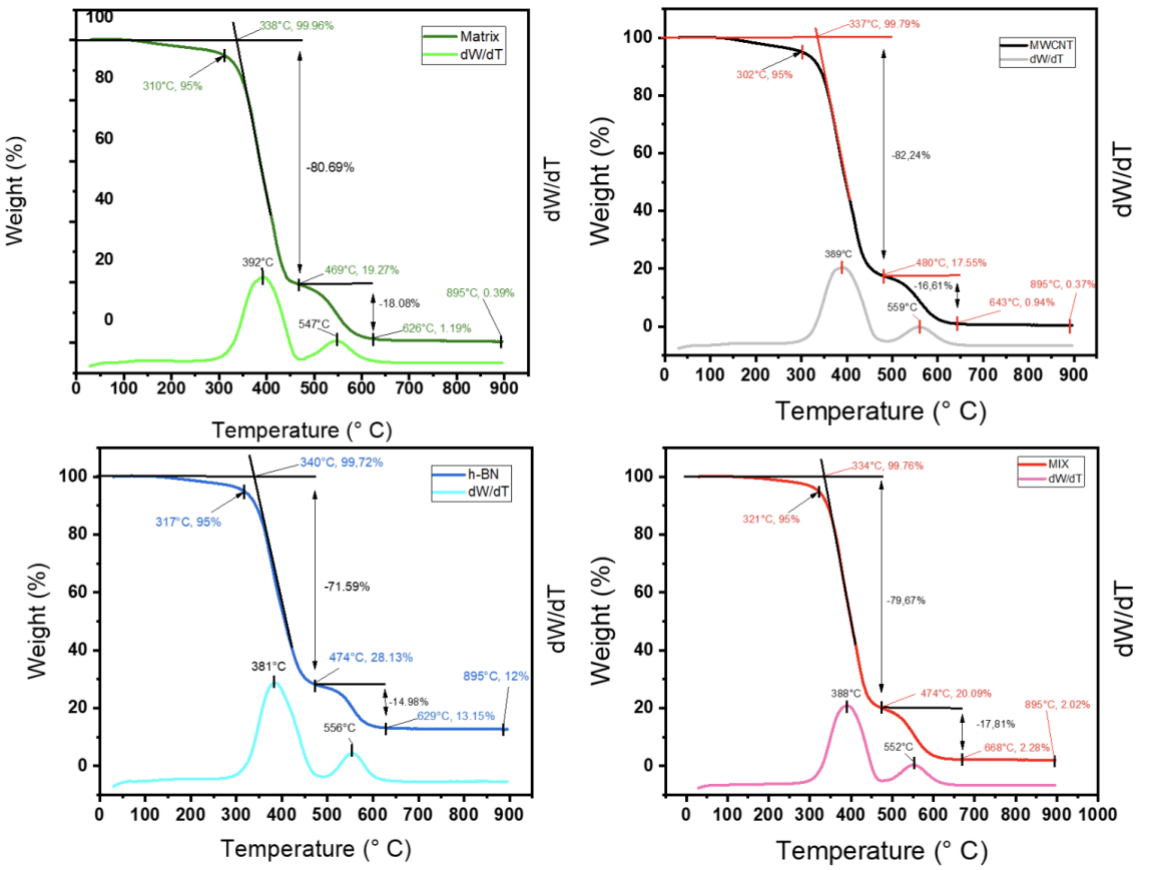


*Figure 20. TGA and DTG curves of the printed formulations, illustrating the thermal degradation behavior and the maximum degradation rate peaks of each sample.*

*Table 9. Summary of thermogravimetric analysis (TGA) parameters of the studied formulations*

| | $T_{5\%}$ [°C] | DTG Peak 1 [°C] | Main Weight Loss [°C] | Residue at 895 °C [°C] |
|---|---|---|---|---|
| **Matrix** | 338 | 392 | 80.71 | 0.39 |
| **h-BN** | 337 | 381 | 71.68 | 12.0 |
| **MWCNT** | 340 | 389 | 81.37 | 0.37 |
| **MIX** | 334 | 388 | 79.67 | 2.02 |

As summarized in *Table 8*, the temperature at 5 wt.% loss (T5%) remained within a narrow range, from 334 to 340 °C. This result suggests that the onset of decomposition is mainly governed by the degradation of the organic resin matrix, while the fillers have only a limited influence on the earliest degradation stage.

The lower mass loss observed for the h-BN sample is consistent with the presence of a larger non-degradable inorganic fraction. In contrast, the MWCNT formulation behaved very similarly to the neat matrix, indicating that the nanotube content was not high enough to

substantially affect the overall degradation yield. The MIX sample showed an intermediate mass loss, slightly lower than the matrix but still much higher than the h-BN system.

The most relevant difference in the formulations was seen in the residue at 895 °C. As expected, the matrix and MWCNT samples exhibited an almost negligible residue level, with values of 0.39% and 0.37%, This confirms that these systems are composed mainly of thermally degradable organic material and that the MWCNT content is too low to have an impact on the final residual mass. In contrast, the h-BN sample retained 12.0% residue, which is coherent with the inorganic and thermally stable nature of boron nitride. However, the MIX formulation showed only 2.02% residue, which is unexpectedly low considering that it should also contain a boron nitride fraction and would therefore be expected to leave a substantially higher inorganic residue.
Since h-BN is thermally stable in this temperature range, the low residue may indicate that the effective amount of h-BN in the analyzed specimen was lower than nominal, possibly due to filler sedimentation, poor dispersion, or local heterogeneity in the sampled portion.

Overall, the TGA results indicate that all materials preserve similar onset thermal stability, while the incorporation of h-BN clearly increases the inorganic residual fraction.
The MWCNT formulation does not significantly alter the degradation behavior relative to the neat matrix, whereas the MIX system exhibits an anomalously low residue, suggesting possible filler–filler or filler–matrix interactions, and compositional heterogeneity within the sample.

### 3.9. Tensile Properties

The tensile behavior of the developed formulations was evaluated both in the as-printed condition and after thermal post-curing in order to assess the effect of filler type and dual-cure network development on mechanical performance. The corresponding tensile curves are shown in *Figure 22*, while the values of ultimate tensile strength (UTS) and Young's modulus (E) are summarized in *Table 9*.

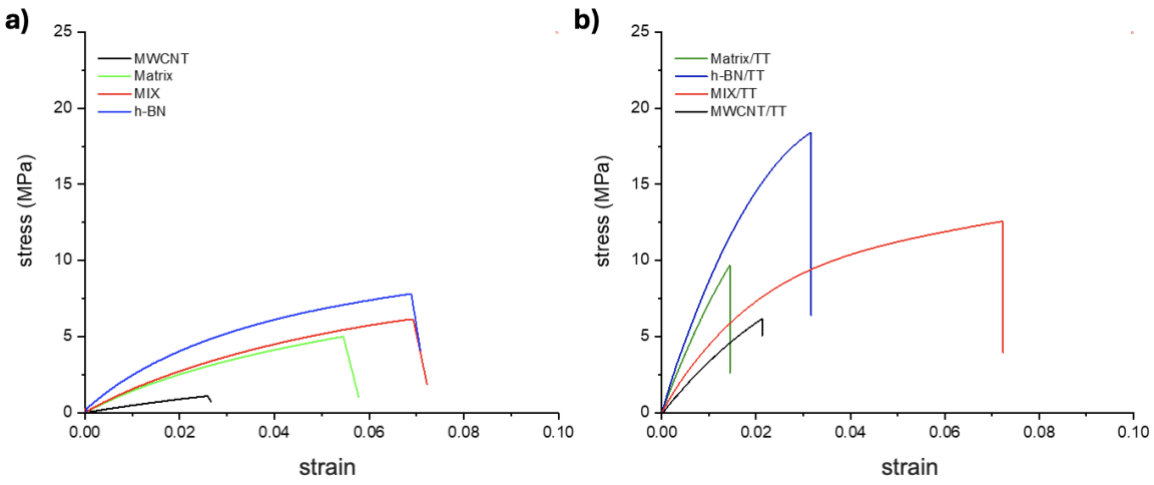


*Figure 21.Stress–strain curves obtained from tensile tests of the studied formulations: (a) samples without thermal treatment and (b) samples after thermal treatment.*

*Table 10. Mechanical properties obtained from tensile tests, including ultimate tensile strength (UTS) and Young's modulus (E) for all formulations*

| | UTS [MPa] | TT-UTS [MPa] | E [MPa] | TT-E [MPa] | Δε [%] | TT-Δε [%] |
|---|---|---|---|---|---|---|
| **Matrix** | 6.5 ± 0.2 | 12.7 ± 2.0 | 141.4 ± 0.4 | 784.7 ± 0.9 | 5.4 ± 0,7 | 1.4 ± 1,1 |
| **MWCNT** | 1.5 ± 0.4 | 5.8 ± 1.9 | 48.0 ± 0.6 | 337.2 ± 1.1 | 2.5 ± 1,0 | 2.1 ± 0,5 |
| **h-BN** | 8.8 ± 2.0 | 19.4 ± 3.9 | 228.1 ± 1.2 | 956.6 ± 2.6 | 6.8 ± 0,6 | 3.1± 0,9 |
| **MIX** | 7.7 ± 2.2 | 13.2 ± 2.0 | 143.9 ± 0.9 | 481.6 ± 2.1 | 6.8 ± 0,9 | 7.2 ± 0,7 |

In the as-printed state, the neat matrix exhibited a UTS of 6.5 MPa and a modulus of 141 MPa, reflecting the mechanical response of the UV-cured acrylate-dominated network before thermal densification. The formulation containing h-BN showed the highest tensile performance among the untreated samples, reaching 8.8 MPa in UTS and 228 MPa in modulus. This behavior indicates that h-BN acts as an effective reinforcing filler, increasing both stiffness and strength due to its rigid ceramic nature and its relatively limited interference with the photopolymerization process.

In contrast, the MWCNT-containing formulation exhibited the lowest tensile performance, with a UTS of only 1.5 MPa and a modulus of 48 MPa. This weak mechanical response is consistent with the lower degree of conversion previously observed by FTIR and the lower

Tg obtained by DMTA, the presence of carbon nanotubes negatively affected the efficiency of UV curing and hindered the formation of a mechanically robust network.

After thermal treatment, a substantial improvement in tensile performance was observed for all available formulations. The neat matrix increased to 12.7 MPa in UTS and 784 MPa in modulus, confirming that the thermal post-curing step significantly enhances network development through a C=C post curing and the activation of the epoxy–amine reaction. The h-BN formulation showed the highest mechanical performance overall, reaching 19.5 MPa in UTS and 956 MPa in modulus. This result indicates that h-BN provides the most effective reinforcement when combined with the thermally completed dual-cure network.

As we can observe in the *Figure 22*, the stress–strain curves show that most formulations displayed a brittle or quasi-brittle mechanical response, with fracture occurring shortly after the initial elastic to nonlinear transition and without a clearly defined plastic flow region. The MIX formulation was the only one showing a more gradual nonlinear deformation, although not enough to establish a well defined yield point in the classical sense.

In general terms, the epoxy groups undergo a ring-opening reaction with the amine hardeners, resulting in a highly crosslinked three-dimensional network with high covalent bonds and reduced free volume. This additional network formation may increase the overall crosslink density, hence providing better stress distribution within the material, resulting in higher tensile strength and modulus [57],[59]. On the other hand, the morphology of the incorporated fillers plays a crucial role in defining the mechanical response of the composites. Hexagonal boron nitride possesses a two-dimensional morphology with a platelet shape that gives a large interfacial area with the polymer matrix, facilitating efficient load transfer and restricting polymer chain mobility [37],[55]. Consequently, the h-BN formulation displays the highest tensile strength and modulus after thermal treatment. Conversely, carbon nanotubes provide a one-dimensional morphology with a high aspect ratio, which is capable of providing effective reinforcement. Nevertheless, their efficacy strongly depends on dispersion quality and interfacial adhesion with the polymer matrix. If these parameters are not entirely realized, nanotubes may act as stress concentration sites,

lowering the mechanical performance of the material. The hybrid formulation containing both h-BN and MWCNT presents an intermediate behavior, indicating that the combined presence of two fillers with different geometries can influence crack propagation mechanisms and deformation behavior, causing to a balance between stiffness and deformability.

### 3.10. Qualitative Thermal Dissipation Analysis.

As research advanced, an infrared thermographic camera was used for a qualitative evaluation of the heat dissipation behavior of the different formulations. The samples were first heated in an oven and subsequently removed and placed on an insulating surface while the temperature evolution was recorded, as shown in *Figure 23,*

The short time required to transfer the samples from the oven to the measurement position, made it impossible to record a perfectly stable initial temperature. As a result, slight variations in the absolute temperature at 0 s were observed between the samples. However, it was observed that the most significant temperature variation occurred within the first seconds after removal from the oven, whereas at longer times the cooling rate became more gradual and relatively similar for all the materials. For this reason, the analysis was conducted comparatively by evaluating both the thermographic images and the temperature decrease over time.

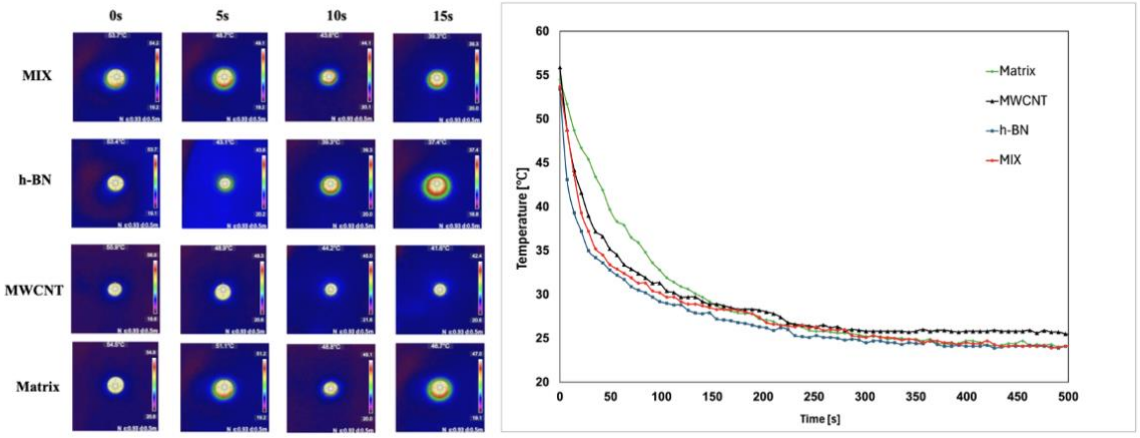


*Figure 22. Infrared thermographic images and temperature evolution during the cooling process of the printed samples measured by thermal camera.*

From the thermographic sequences, it can be observed that the filled systems exhibit a more pronounced temperature variation during the first seconds compared to the neat matrix. In particular, the formulations containing h-BN and the hybrid MIX system show larger temperature dissipation in the early stage of cooling, This observation suggests a more efficient heat redistribution and dissipation within the material. In contrast, the neat matrix shows a smaller temperature variation over the same time interval, indicating a slower thermal response.

These findings are support the expected effect of thermally conductive fillers. It is noticeable that hexagonal boron nitride is well known for its high intrinsic thermal conductivity and its capacity to promote heat transport within polymer matrices, while carbon nanotubes can also contribute to heat transfer through their high aspect ratio and conductive pathways. The combined system (MIX) appears to benefit from the presence of both fillers, which may facilitate the formation of partial thermal transport networks within the polymer matrix.

It should be emphasized that this thermographic test was developed under non-steady-state cooling conditions and involved manual transfer of the samples from the oven to the measurement surface.

Therefore, for the results in this specific phenomenon heat dissipation behavior should be interpreted based on a qualitative comparison rather than a quantitative measurement of thermal conductivity.

# Chapter 4: Conclusion

This paper presents the research work developed in relation to a dual-cure photopolymerizable hybrid resin system which is strengthened by means of inorganic nanomaterials for usage in vat photopolymerization additive fabrication. The principal objective was to reinforce the thermal and mechanical performance of conventional photopolymer resins, at the same time keeping compatibility with LCD-based printing processes.

The formulation developed mixed a UV-curable acrylate matrix with a thermally activated epoxy–amine network. This dual-curing method permitted a rapid shape fixation process during the printing process by means of radical photopolymerization, followed by additional network formation during thermal post-curing. The procedure of confirmation of thermal analysis showed that the epoxy-amine reaction took place in the temperature range established by DSC, and the recession of the epoxy signal in FTIR spectra corroborated the outstanding realization of the secondary curing reaction. Subsequently, all formulations showed an increment in glass transition temperature and increased thermomechanical stability after thermal treatment.

From the perspective of the process, the rheological analysis showed that all of the formulations stayed within a viscosity range compatible with vat photopolymerization processes. Despite the fact that the presence of fillers augmented viscosity and introduced shear-thinning behavior, it is possible to argue that this reaction was favorable for sustaining suspension stability while allowing adequate resin flow while recoating.

The analysis of the Jacobs working curve brought to light that nanofillers substantially lowered light penetration depth as a result of scattering and absorption phenomena. Nonetheless, the successful printing of all formulations was enabled through the right adjustment of exposure parameters. This success in printing confirmed the usefulness of producing nanocomposite structures using LCD-based additive manufacturing.

The addition of inorganic nanofillers influenced importantly the behavior of the material. Hexagonal boron nitride exhibited the most effective reinforcement effect, resulting in the highest tensile strength and modulus after post-curing. This enhancement is assigned to the platelet morphology of h-BN, that boosts effective stress transfer within the polymer matrix and contributes to network stability. On the other hand, the displayed formulation that contains multi-walled carbon nanotubes reduced curing efficiency and lower mechanical performance, associated to the light absorption effects that limit photopolymerization during printing as well as to the strong tendency of CNTs to agglomerate due to van der Waals interactions. Such agglomeration blocks homogeneous dispersion within the polymer matrix taking to the formation of localized clusters that can act as stress concentration sites and

further lower the effectiveness of load transfer within the network. The hybrid filler system showed intermediate mechanical behavior, implying that interactions among fillers have an influence in network formation and deformation mechanisms.

The thermogravimetric analysis registered thermal degradation onset temperatures for all systems, proposing that nanofillers incorporation did not alter the primary degradation mechanism of the polymer matrix at a substantial level. Nevertheless, the h-BN formulation showed a higher inorganic residue, dealing with the presence of thermally stable ceramic filler.

In summary, qualitative thermographic assessment display that filler-containing formulations expose faster temperature decay during cooling compared to the neat matrix, this shows heat dissipation behavior. This study suggests that the implementation of thermally conductive fillers help to improved thermal transport withing the material, nevertheless, it is necessary to go further to a quantitative analysis to provide thermal conductivity values.

In general, the results test that hybrid dual-cure photopolymer systems strengthened with thermally conductive nanomaterials represent an encouraging strategy for developing functional materials, appropriately, for vat photopolymerization processes. It is worth mentioning that the most favorable balance between printability, mechanical performance and thermal response were shown in h-BN reinforced systems.

Research that is aimed for the future should mainly be centered on optimizing filler dispersion, improving filler matrix interfacial interactions, and developing thermal conductivity quantitative measurements for further evaluation of the potential of these materials for thermal management applications in additive manufacturing.

# References


1. Additive manufacturing: A comprehensive review. (2024). *Sensors*. https://doi.org/10.3390/s24092668
2. Zhang, Y., Li, X., Wang, J., Liu, H., & Chen, Q. (2023). Thermally conductive polymer composites filled with boron nitride for advanced thermal management applications. *Polymers, 18*(2), 192. https://doi.org/10.3390/polym18020192
3. Walia, K., Khan, A., & Breedon, P. (2021). Polymer-based additive manufacturing: Process optimisation for low-cost industrial robotics manufacture. *Polymers, 13*(16), 2809. https://doi.org/10.3390/polym13162809
4. Petrillo, A., et al. (2022). Spare parts made by additive manufacturing to improve preventive maintenance. *Applied Sciences*.
5. ASTM International. (2012). *Standard terminology for additive manufacturing technologies (ASTM F2792-12a).* ASTM International.
6. ISO/ASTM. (2015). *Additive manufacturing — General principles — Terminology (ISO/ASTM 52900:2015).* ISO/ASTM.
7. Baumers, M., Tuck, C., & Hague, R. (2022). Spare parts made by additive manufacturing to improve preventive maintenance. https://www.researchgate.net/publication/364392239
8. Maresca, D., et al. (2024). Advances in additive manufacturing for medical imaging and biomedical applications. *EJNMMI Physics*. https://doi.org/10.1186/s40580-024-00452-3
9. Snyder, J. (2019). Adding 3D printing to manufacturing. *Digital Engineering 24/7*. https://www.digitalengineering247.com/article/adding-3d-printing-to-manufacturing
10. Jain, R. (2020). Laser SLA vs DLP vs masked SLA: 3D printing technology compared. *The Orthocosmos*. https://theorthocosmos.com/laser-sla-vs-dlp-vs-masked-sla-3d-printing-technology-compared/
11. Frost, M. C., & Ranjan, R. (2024). Novel and rapid analytical platform development enabled by advances in 3D printing. *Frontiers in Analytical Science, 4*. https://doi.org/10.3389/frans.2024.1505510

12. Zhang, H., Li, Y., Chen, X., Wang, J., & Liu, Z. (2024). Recent advances in thermally conductive polymer composites for thermal management applications. *Additive Manufacturing Letters, 9*, 100188. https://doi.org/10.1016/j.addlet.2024.100188
13. Center for Bits and Atoms. (2024). *Vat photopolymerization*. Massachusetts Institute of Technology. https://fab.cba.mit.edu/classes/865.24/topics/additive/pages/vatpoly.html
14. Pagac, M., Hajnys, J., Ma, Q. P., Jancar, L., Jansa, J., Stefek, P., & Mesicek, J. (2021). A review of vat photopolymerization technology: Materials, applications, challenges, and future trends of 3D printing. *Polymers, 13*(4), 598. https://doi.org/10.3390/polym13040598
15. Formlabs. (2023). *SLA vs. DLP: Comparing resin 3D printing technologies*. https://formlabs.com/blog/resin-3d-printer-comparison-sla-vs-dlp/
16. Khecho, A., Rahman, M. M. T., Reddy, D., El-Ghannam, A., & Joyee, E. B. (2025). DLP-based additive manufacturing of hollow 3D structures with surface activated silicon carbide–polymer composite. *Composites Part B: Engineering, 296*, 112236. https://doi.org/10.1016/j.compositesb.2025.112236
17. Ambrosi, A., & Pumera, M. (2018). 3D-printing technologies for electrochemical applications. *ACS Applied Polymer Materials, 1*(1), 2–17. https://doi.org/10.1021/acsapm.8b00165
18. Nam, J., & Kim, M. (2024). Advances in materials and technologies for digital light processing 3D printing. *Nano Convergence, 11*, 45. https://doi.org/10.1186/s40580-024-00452-3
19. Gurr, M., Hofmann, D., Ehm, M., Thomann, Y., Kübler, R., Mülhaupt, R., & Liska, R. (2023). From resin formulation and process parameters to the final mechanical properties of 3D printed acrylate materials. https://www.researchgate.net/publication/369480285
20. Ligon, S. C., Liska, R., Stampfl, J., Gurr, M., & Mülhaupt, R. (2017). Polymers for 3D printing and customized additive manufacturing. *Chemical Reviews, 117*(15), 10212–10290. https://doi.org/10.1021/acs.chemrev.7b00074

21. Bagheri, A., & Jin, J. (2021). Photopolymerization in 3D printing. *Progress in Polymer Science, 112*, 101353. https://doi.org/10.1016/j.progpolymsci.2020.101353
22. Muñoz, J., & Pumera, M. (2020). Vat photopolymerization 3D printing of conductive nanocomposites. *Chemical Society Reviews*.
23. Ngo, T. D., Kashani, A., Imbalzano, G., Nguyen, K. T. Q., & Hui, D. (2018). Additive manufacturing (3D printing): A review of materials, methods, applications and challenges. *Composites Part B: Engineering, 143*, 172–196. https://doi.org/10.1016/j.compositesb.2018.02.012
24. Sangermano, M. (2012). Advances in cationic photopolymerization and dual-curing systems. *Progress in Polymer Science, 37*(1), 127–143. https://doi.org/10.1016/j.progpolymsci.2011.08.001
25. Gibson, I., Rosen, D., & Stucker, B. (2015). *Additive manufacturing technologies: 3D printing, rapid prototyping, and direct digital manufacturing* (2nd ed.). Springer.
26. Decker, C. (2009). Photoinitiated crosslinking polymerisation. *Progress in Polymer Science, 34*(7), 705–745.
27. Zhou, X., et al. (2023). Recent advances in photopolymerization-based 3D printing technologies. *Additive Manufacturing*. https://doi.org/10.1016/j.addma.2023.103517
28. Zhao, X., et al. (2002). Understanding the basic principles of polymer chemistry. *Journal of Chemical Education, 79*(6), 715–720.
29. Chen, H., Ginzburg, V. V., Yang, J., Yang, Y., Liu, W., Huang, Y., Du, L., & Chen, B. (2016). Thermal conductivity of polymer-based composites: Fundamentals and applications. *Progress in Polymer Science, 59*, 41–85. https://doi.org/10.1016/j.progpolymsci.2016.03.001
30. Zhao, Z., Li, Y., Liu, Z., et al. (2020). Materials for additive manufacturing with enhanced functionality. *Progress in Materials Science, 100*, 557–603.
31. Zha, J. W., Wang, F., & Wan, B. (2025). Polymer composites with high thermal conductivity: Theory, simulation, structure and interfacial regulation. *Progress in Materials Science, 148*. https://doi.org/10.1016/j.pmatsci.2024.101362
32. Tilve-Martinez, D., & Poulin, P. (2025). Vat photopolymerization 3D printing of conductive nanocomposites. *Accounts of Materials Research, 6*(5), 661–671. https://doi.org/10.1021/accountsmr.5c00060

33. Zhou, X., Li, Y., & Wang, Y. (2023). Thermal conductive polymer composites: Recent progress and applications. *Journal of Materials Science & Technology*.
34. Zhang, H., Chen, H., & Luo, J. (2020). Thermal conductive polymer composites: Classification, design, and applications. *Advanced Engineering Materials, 22*(2), 1901307. https://doi.org/10.1002/adem.201901307
35. Zhang, X., et al. (2007). Polymer composite materials: Thermal and mechanical performance. *Journal of Chemical Education, 84*(8), 1295–1301.
36. Gu, J., Zhang, Q., Dang, J., & Yang, Z. (2018). Thermal conductivity enhancement in polymer composites with hybrid fillers. *Progress in Polymer Science, 81*, 1–29. https://doi.org/10.1016/j.progpolymsci.2018.03.002
37. Raman, C. (2008). Boron nitride in thermoplastics: Effect of loading, particle morphology and processing conditions. *NATAS Annual Conference on Thermal Analysis and Application*.
38. Moniruzzaman, M., & Winey, K. I. (2006). Carbon nanotubes in polymer composites. *Macromolecules, 39*, 5194–5205.
39. Ossila. (2024). What are multi-walled carbon nanotubes? https://www.ossila.com/pages/what-are-multi-walled-carbon-nanotubes
40. OCSiAl. (n.d.). Multi-walled carbon nanotubes. https://tuball.com/articles/multi-walled-carbon-nanotubes
41. Kuriger, R., & Alam, M. (2002). Experimental study of thermal conductivity in polymer composites. *Experimental Heat Transfer, 15*, 19–30.
42. Zhou, Y., Li, X., Zhang, H., Wang, J., & Liu, Z. (2022). Carbon nanotube-based polymer nanocomposites: A review of mechanical and thermal properties. *Nanomaterials, 12*(20), 3574. https://doi.org/10.3390/nano12203574
43. Liqcreate. (2023). Cure depth of resin: Ec, Dp and curing behavior. https://www.liqcreate.com
44. Kimteks. (2024). Allyl glycidyl ether (AGE). https://www.kimteks.com.tr/en/age/
45. Smith, J., & Doe, A. (2016). The synthesis of allyl glycidyl ether copolymers and their thermokinetic analysis. *Journal of Polymer Science, 54*(12), 1500–1515.
46. Wang, L., & Zhang, Q. (2017). Thermal properties and kinetics of allyl glycidyl ether polymers. *Polymer International, 66*(7), 865–874. https://doi.org/10.1002/pi.6436

47. Lin, Y., Deng, W., Rui, Y., Liu, Y., Lu, G., & Liu, J. (2022). Enhanced thermal conductivity of epoxy acrylate/h-BN and AlN composites by photo-curing 3D printing technology. *Journal of Applied Polymer Science, 139*(29). https://doi.org/10.1002/app.52629
48. Poompiew, N., et al. (2023). 3D printable resin/carbon nanotube composites for wearable strain sensors. *Journal of Science: Advanced Materials and Devices, 8*(2). https://doi.org/10.1016/j.jsamd.2023.100546
49. Hisham, M., et al. (2024). Additive manufacturing of carbon nanocomposites for structural applications. *Journal of Materials Research and Technology, 28*, 4674–4693. https://doi.org/10.1016/j.jmrt.2024.01.049
50. Weng, Z., et al. (2023). 3D printing of ultra-high viscosity resin by a linear scan-based vat photopolymerization system. *Nature Communications, 14*, 4303.
51. Šimunović, L., et al. (2025). Rheology of dental photopolymers for SLA/DLP/MSLA 3D printing. *Polymers, 17*(19), 2706. https://doi.org/10.3390/polym17192706
52. Decker, C., & Moussa, K. (2016). Carbon nanotube-based UV-curable nanocomposite coatings. *Progress in Organic Coatings, 92*, 122–128. https://doi.org/10.1016/j.porgcoat.2015.12.003
53. Gu, J., et al. (2017). Thermally conductive polymer composites with boron nitride fillers. *Progress in Polymer Science, 64*, 1–38. https://doi.org/10.1016/j.progpolymsci.2016.10.002
54. Tumbleston, J. R., et al. (2015). Continuous liquid interface production of 3D objects. *Science, 347*, 1349–1352. https://doi.org/10.1126/science.aaa2397
55. Pascault, J. P., & Williams, R. J. J. (2010). *Epoxy polymers: New materials and innovations*. Wiley-VCH.
56. Zanon, M. (2023). *Photocurable hydrogels for tissue engineering applications and 3D printing* (PhD dissertation). Politecnico di Torino.
57. Applied Poleramic. (n.d.). Amine-cured epoxy matrices: Technical notes. https://www.appliedpoleramic.com/amine-cured-epoxy-matrices-technical-notes.html
58. Balandin, A. A. (2007). Thermal properties of graphene and nanostructured carbon materials. arXiv. https://arxiv.org/pdf/cond-mat/0701607

59. Spitalsky, Z., Tasis, D., Papagelis, K., & Galiotis, C. (2010). Carbon nanotube–polymer composites: Chemistry, processing, mechanical and electrical properties. *Progress in Polymer Science, 35*(3), 357–401. https://doi.org/10.1016/j.progpolymsci.2009.09.003

60. Liu, Y. Zhang, Z. Li, et al., *"CNT-Reinforced Self-Healable Epoxy Dynamic Networks Based on Disulfide Bond Exchange,"* **Polymers,** vol. 14, 2022. https://doi.org/10.3390/polym14235250

61. Esmizadeh, E., Yousefi, A. A., & Naderi, G. (2014). Effect of type and aspect ratio of different carbon nanotubes on cure behavior of epoxy-based nanocomposites. *Iranian Polymer Journal, 24*(1), 1–12. https://doi.org/10.1007/s13726-014-0281-4

62. Borgert, M., De Simone Cividanes, L., Simonetti, E. A. N., & Fernandes, F. W. (2014). Influence of carbon nanotubes on epoxy resin cure reaction using different techniques: A comprehensive review. *Polymer Engineering & Science, 54*(11). https://doi.org/10.1002/pen.23775

63. Hutchinson, J. M., & Moradi, S. (2020). Thermal conductivity and cure kinetics of epoxy–boron nitride composites—A review. *Materials, 13*(16), 3634. https://doi.org/10.3390/ma13163634

64. Moradi, S.; Calventus, Y.; Román, F.; Hutchinson, J. M. Achieving high thermal conductivity in epoxy composites: Effect of boron nitride particle size and matrix–filler interface. *Polymers* 2019, 11, 1156. https://doi.org/10.3390/polym11071156